Simulation of TRMM Microwave Imager Brightness Temperature Using Precipitation Radar Reflectivity for Convective and Stratiform Rain Areas Over Land

C. Prabhakara
NASA Goddard Space Flight Center, Greenbelt, Maryland

R. Iacovazzi, Jr.
Science Systems and Applications, Inc., Lanham, Maryland

J.-M. Yoo
EWHA Womans University, Seoul, South Korea

February 2002

Abstract

Observations of brightness temperature, Tb, made over land regions by the Tropical Rainfall Measuring Mission (TRMM) Microwave Imager (TMI) radiometer have been analyzed along with the nearly simultaneous measurements of the vertical profiles of reflectivity factor, Z, made by the Precipitation Radar (PR) onboard the TRMM satellite. This analysis is performed to explore the interrelationship between the TMI and PR data in areas that are covered predominantly by convective or stratiform rain. In particular, we have compared on a scale of 20 km, average vertical profiles of Z with the averages of Tbs in the horizontal polarization of the 19, 37 and 85 GHz channels, i.e T19, T37, and T85. Generally, we find from these data that as Z increases, Tbs in the three channels decrease due to extinction. In order to explain physically the relationship between the Tb and Z observations, we have performed radiative transfer simulations utilizing vertical profiles of hydrometeors applicable to convective and stratiform rain regions. These profiles are constructed taking guidance from the Z observations of PR and recent LDR and Z_{DR} measurements made by land-based polarimetric radars.

We find that the hydrometeor particle size distribution plays an important role in both the convective and stratiform simulations. In the convective model, a significant mixed layer of water and ice particles above the freezing level is necessary to simulate Tbs satisfactorily. In the stratiform model, the density of ice aggregates (snow flakes), which varies inversely with respect to the square of the particle diameter, is required. Also, the emission due to melting snow flakes below the freezing level is needed. The differences in the viewing geometry between PR and TMI could affect the quality of the

simulations. This issue is not addressed here. In this study, we demonstrate that the T85, T37, and T19 observations of TMI in the convective areas can be simulated crudely from the observations of Z. However, for the stratiform region, only simulations of T85 are of comparable quality. The T37 and T19 observations are not as well simulated because of the uncertainties of the modeling of the melting layer, and also contamination introduced by the surface emission. This investigation indicates that the TMI 85 GHz channel yields the best information about rain over tropical land because it has minimal surface contamination, strong extinction, and a fine footprint. The brightness temperature difference (T19-T37) can supplement the information given by the 85 GHz channel in the convective rain areas.

1. Introduction

In atmospheric columns with convective rain, the nature of hydrometeors has been observed to differ significantly from that in columns with stratiform rain (e.g., Houze, 1993, 1997). This is mainly because of differences in the dynamics associated with these two rain types. In convective regions, low-level convergence of moist air results in buoyant updrafts that can have speeds of several ms^{-1}. Furthermore, in convection the rain drops grow by the collision-coalescence mechanism primarily below the freezing level. Above the freezing level, the relatively strong vertical motions lead to a layer containing water and ice particles in mixed-phased form (see Smith et al., 1999; Bringi et al., 1997; Balakrishnan and Zrnic, 1990; and Sax and Keller, 1980). Radar reflectivity factor, Z (hereafter termed reflectivity), measurements in the convective regime indicate an appreciable variability in the horizontal. The typical scale of convective cells is on the order of a few kilometers. However, these cells often exist together on a scale of about 20 km, which corresponds to that of thunderstorms (Cbs). Thus, to get fine information about convective rain, an observing instrument should have a field of view (*fov*) of about 2 km. If an instrument has a resolution that is poorer than this, details of the Cbs can be perceived only in a crude fashion.

In contrast to the dynamics associated with convective rain, in stratiform rain regions there is weak mesoscale convergence near cloud base, which leads to weak rising motion above (Houze, 1997). Radar reflectivity measurements show that in the stratiform rain regime there is a relatively uniform distribution of hydrometeors in the horizontal. The growth of hydrometeors takes place mainly above the freezing level, and is due to deposition of water vapor onto slowly-falling ice particles that form large,

3

low-density ice aggregates (snow flakes) (see Sekhon and Srivastava, 1970). In stratiform rain regions, the mixed-phase layer above the freezing level is not prominent due to weak vertical motions. Below that level, snow flakes melt within about a distance of 500 m. Under favorable conditions, this melting layer manifests itself as a "bright band", or peak, in the radar reflectivity profile. Beneath this layer, rain drops essentially originate from the relatively-large snow flakes that have fully melted. For a given rain rate, it is found that the mode diameter of drop size present in stratiform rain is larger than that in convective rain (see Short et al., 1997). In the estimation of near-surface rain rate, R, based on radar reflectivity, this difference in drop size distribution between convective and stratiform rain is incorporated in the form of separate Z-R relationships.

From the above discussion, it follows that the presence of a bright band in the vertical profile of Z, and/or horizontal variability of Z, is needed to infer rain type. Given this information one can estimate rain rate using an appropriate Z-R relationship (e.g., Iguchi et al., 2000). In the case of passive microwave radiometer observations, local minima in 85 GHz brightness temperature, T85, can be used to discriminate crudely convective rain from stratiform rain. Then, in a manner similar to radar, empirical T85-R relationships could be developed to retrieve convective and stratiform rain rates from microwave radiometer data (Prabhakara et al., 2000, from hereafter PIWD). An analogous approach was implemented by Adler and Negri (1988) to estimate convective and stratiform rain rates from satellite infrared radiometer data.

In this study, in order to appreciate the connection between radar and passive microwave radiometer observations, we have analyzed the nearly simultaneous

4

measurements of the Tropical Rainfall Measuring Mission (TRMM) Microwave Imager (TMI) radiometer and Precipitation Radar (PR) onboard the TRMM satellite. In particular, we have compared the vertical profiles of Z given by the PR with the brightness temperatures, Tbs, in the horizontal polarization of the 19, 37, and 85 GHz - i.e., T19, T37, and T85 - measured by the TMI. This is done separately for the convective and stratiform rain areas discriminated by the PR. Then, in order to explain theoretically the connection between the profiles of Z and the Tbs, we have developed separate radiative transfer models applicable to convective and stratiform rain regions. From this investigation, we can infer the relative importance of different channels of the TMI radiometer for the purpose of rain retrieval over land.

2. Correspondence Between TMI and PR Observations of Convective and Stratiform Rain Over Land

The near-surface rain rate deduced from PR observations has a horizontal resolution of about 4.3 km x 4.3 km. These PR data are arranged uniformly at a spacing of about 4.3 km both along and across scan lines. On the other hand, the footprints of the TMI 85 GHz vertical and horizontal polarization channels are approximately 5.0 km x 7.0 km, and are separated by about 5.0 km along scan lines and about 14 km across scan lines. This scan pattern degrades the effective resolution of the TMI 85 GHz channel compared to that of the PR. The TMI radiometer contains additional channels in vertical and horizontal polarization near 10, 19, and 37 GHz that have a resolution of about 40, 20, and 10 km, respectively. Furthermore, TMI has a 21 GHz channel in vertical polarization that has a resolution similar to that of 19 GHz. In this study, we are scrutinizing the information given by the PR and the TMI in the 19, 37, and 85 GHz
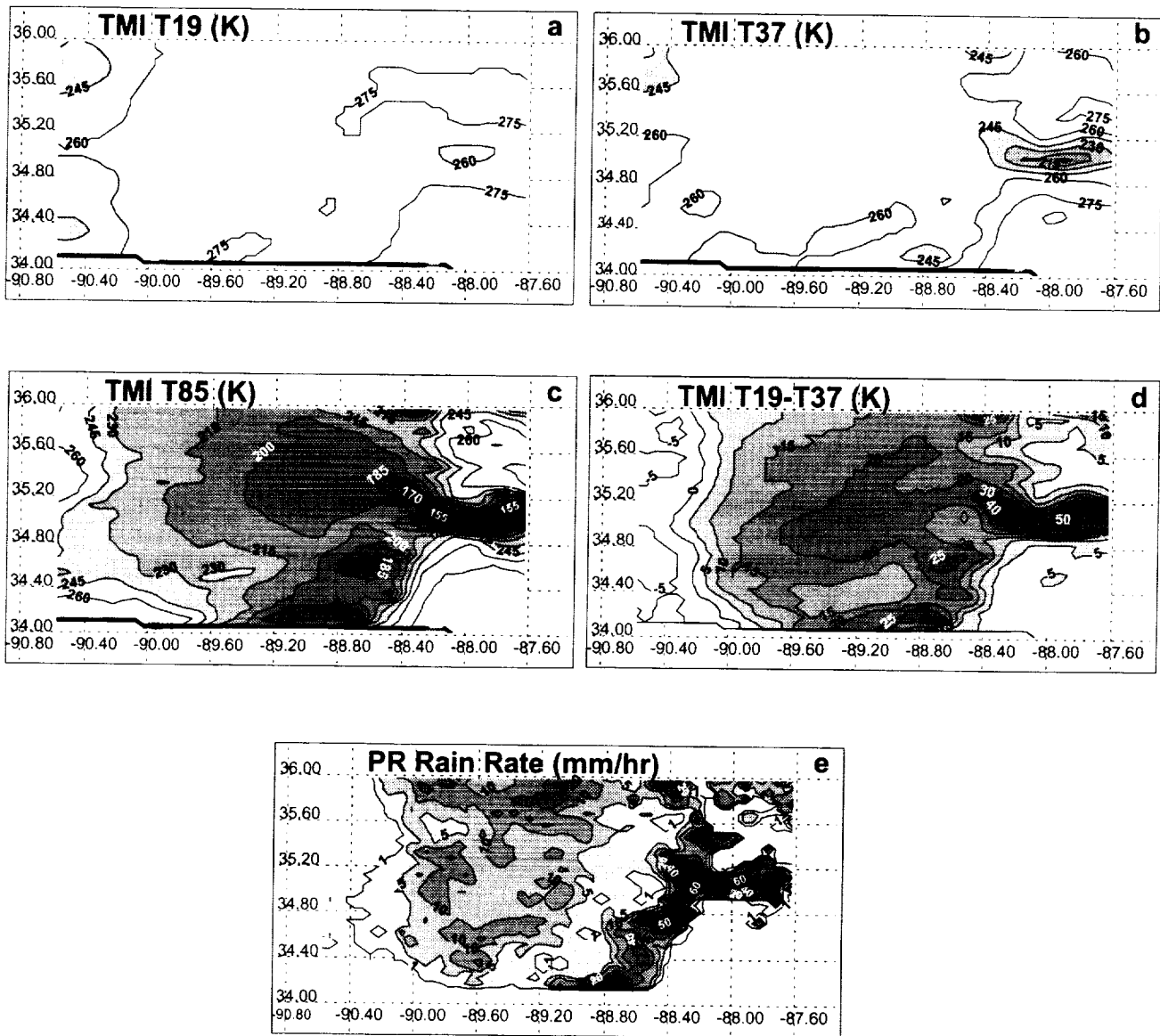
Figure 1: Maps of **a)** T19, **b)** T37, **c)** T85, **d)** (T19-T37), and **e)** PR near-surface rain rate for a mesoscale convective system observed by the TRMM satellite on 5 June 1998 over the Southeast United States.

channels. The TMI 10 and 21 GHz channels are not included in this investigation. This is because the 10 GHz channel has a relatively large footprint, and the information given by the 21 GHz channel is very similar to that of 19 GHz. Also, we consider only the horizontal polarization measurements made by TMI, because they tend to have a larger dynamic range compared to vertical polarization measurements.

In Figures 1a-e, we show maps of T19, T37, T85, and (T19-T37), as well as a map of PR near-surface rain rate, for a mesoscale convective system (MCS) that occurred over the Southeast United States on 5 June 1998. From these figures, we note that the spatial distribution of PR rain rate compares well with that of T85, but not with that of T19 or T37. In the 19 GHz panel, the minimum of 245 K seen in the northwest corner is essentially due to wet surface, and the minimum of 260 K seen toward the east is rain related. These features may be noticed in the 37 GHz panel with a different emphasis on wet land and rain. In the 85 GHz panel, the wet surface influence is not apparent. This illustrates that the lower frequency channels on land are significantly contaminated by surface emissivity variations. However, a map of the difference, (T19-T37), which reduces this surface contamination, produces a good comparison with the PR rain rate patterns. Such information given by the microwave radiometer and the radar is noticed over widely different regions of the tropics.

We show in Figure 2a a vertical cross section of the radar reflectivity taken from TRMM PR along a sub-satellite track. This cross section, which starts at ($35.1°$ N, $90.6°$ W) and ends at ($35.0°$ N, $87.6°$ W), corresponds to the same MCS depicted in Figs. 1a-e. The PR reflectivity below the 1 km level is not shown in this figure to avoid problems related to signal clutter arising from surface topography. We note from Fig. 2a that the
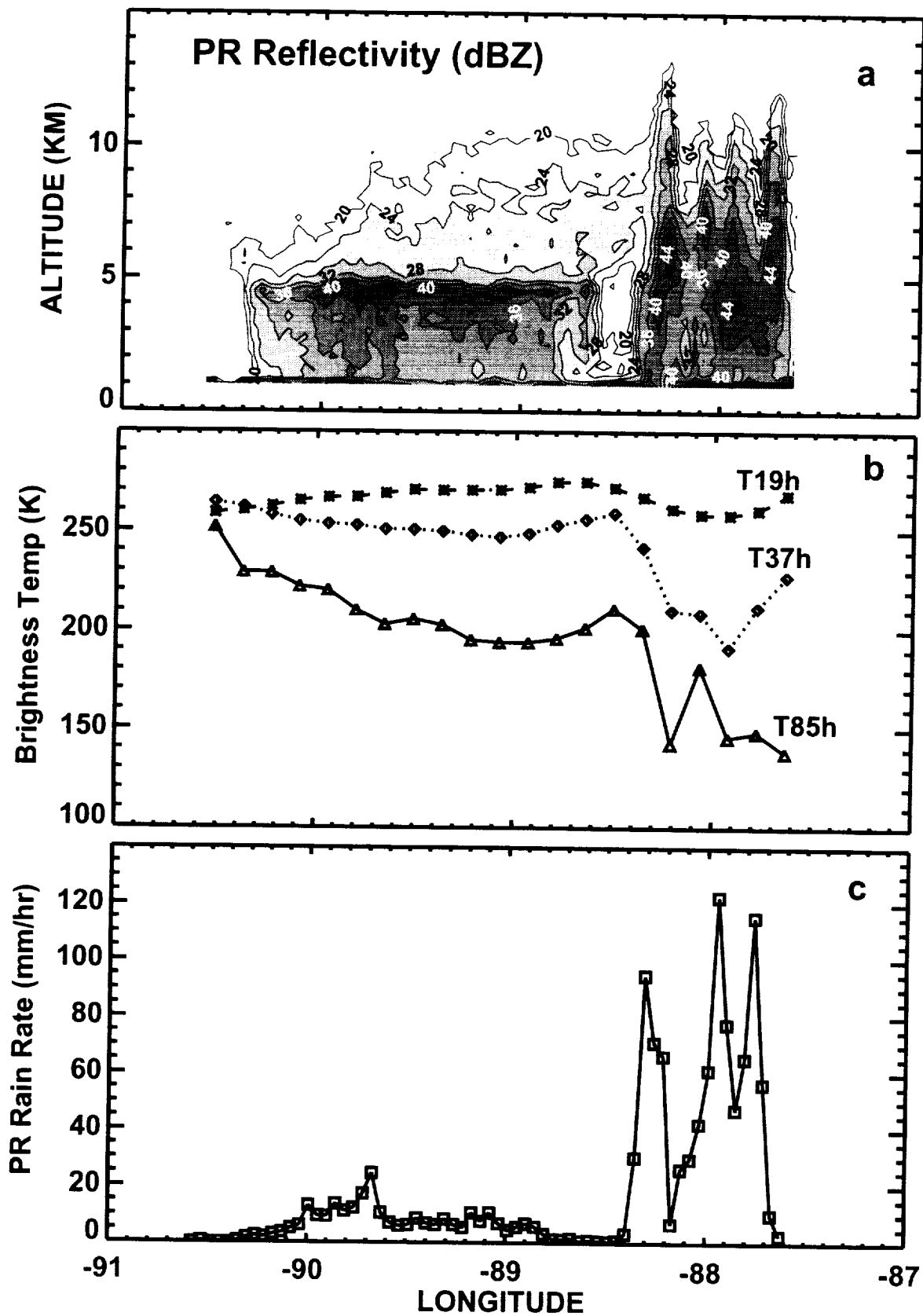
7

Figure 2: Vertical cross-sections of **a)** PR reflectivity, **b)** TMI T19, T37, and T85, and **c)** PR near-surface rain rate for the MCS presented in Figure 1. Note that these observations represent those from the TRMM sub-satellite track.

leading edge of the storm, with its tall convective towers, is near 88° W. High reflectivity cores (> 30 dBZ) that extend well above the freezing level (~5.0 km) characterize these convective towers. To the west of these convective towers, from 88.6° W to 90.3° W, and above the freezing level, we notice an extensive anvil cloud with an almost horizontally uniform pattern of reflectivity. Below the freezing level, underneath the anvil cloud, there is a bright band that is about 0.5 km in thickness. Strong reflectivity in the bright band is attributed to large, low-density melting snow flakes, while the strong reflectivity above the freezing level in the cores of the convective towers is attributed to small, water-coated dense graupel (Bauer et al., 2000). Near the surface, there is intense convective rain in the convective towers, while there is relatively light stratiform rain underneath the anvil (see Figure 2c). Notice there is a small region referred to as the Bounded Weak Echo Region (BWER) between 88.4° W and 88.5° W in the layer from 2 km to 6 km, which is at the origin of the anvil cloud. Such a BWER has been described in earlier studies with the help of observations made by ground-based radars (see Houze, 1993). This description of the reflectivity pattern and rain rate associated with a MCS is helpful in relating the TRMM PR observations with those of TMI.

In Figure 2b the brightness temperatures measured by TMI in the 85, 37 and 19 GHz channels are shown along the sub-satellite track to correspond to the cross section of PR reflectivity shown in Fig. 2a. In the response of the 85 GHz channel, we find there is a strong scattering depression due to relatively dense ice particles where the convective towers are present, but some of the individual towers are not well resolved. The anvil in the stratiform region produces weaker scattering depression. Over the entire cross-section domain, the response of the 37 GHz channel is similar to that of the

9

85 GHz channel, except that the scattering depression in 37 GHz is not as strong. The response in the 19 GHz channel is the weakest of the three channels. The interrelationship between TMI measured T85, T37, and T19, and the PR measured Z and R, is only crudely reflected in Figs. 2a-c, because of differences in the resolution of the TMI and PR data.

To compare the TMI and PR data sets, we have averaged them to one spatial scale, which corresponds to the 19 GHz *fov*. This scale is about 20 km, which is similar to the scale of Cbs. Averaging the TMI and PR data to this scale helps also to alleviate problems introduced by the differences in the viewing geometry (see also Hong et al., 2000) of these two instruments. The TMI has a conical scanning geometry, while the PR has a cross-track scanning geometry. The PR data near the surface is generally used to deduce rain information. On the contrary, the 85 GHz temperature responds to the hydrometeors in the whole column of the atmosphere, with special emphasis on ice hydrometeors above the freezing level (Wu and Weinman, 1984). Thus, differential advection of hydrometeors between the upper and lower levels can create spatial mismatch between the 85 GHz data of TMI and PR near-surface rain observations. Also, the hydrometeors originating at higher altitudes take several minutes to reach the surface. For these reasons, averaging the data of each instrument to the scale of the 19 GHz *fov* will reduce the problems involved in comparing the information content of these two datasets. Similar arguments also apply to the 37 GHz data. However, compared to the 85 GHz, the 37 GHz channel responds to lower layers of the atmosphere, while the 19 GHz channel is sensitive to layers even further below.

Table 1: The date, time, and location for 20 MCS events over land observed by the TRMM satellite. Also given are the number of convective and stratiform pixels for each rain event.

Number	Month	Day	Time	Lat	Long	Region	# Conv Pixels	# Strat Pixels
1	'98 Jan	9	528	-4.65	-74.20	Amazon	3	94
2	'99 Jan	19	1820	-17.90	29.75	Africa	1	24
3	'99 Feb	13	1431	-17.20	127.50	Australia	12	13
4	'98 Jun	5	708	32.75	-92.00	USA	10	1
5	'98 Jun	5	845	35.00	-89.10	USA	27	40
6	'98 Jun	8	2010	12.50	-1.40	Africa	5	11
7	'98 Jun	9	1030	4.40	-66.20	Amazon	0	62
8	'98 Jun	11	441	33.00	-99.50	USA	13	14
9	'98 Jun	18	1500	26.90	115.70	China	3	66
10	'98 Jun	20	1411	25.80	115.00	China	4	17
11	'98 Jun	29	456	32.75	116.00	China	12	19
12	'98 Jul	1	829	12.20	-2.20	Africa	12	27
13	'98 Jul	5	223	24.00	81.50	India	7	29
14	'98 Jul	20	1648	28.90	116.00	China	2	18
15	'98 Jul	20	2247	17.80	-0.05	Africa	20	27
16	'99 Jul	11	157	25.00	84.10	India	14	54
17	'99 Jul	22	405	4.60	-69.30	Amazon	11	17
18	'99 Jul	29	2018	14.45	2.50	Africa	13	15
19	'99 Sep	16	413	34.20	-78.20	USA	11	62
20	'98 Dec	28	1034	-26.70	-58.00	South America	30	40

Based on the arguments presented above, we have assumed that averaging the TMI 85 and 37 GHz data to the 19 GHz *fov*, will be suitable for this study. A similar averaging is also applied to the PR measured reflectivity, Z, at several discrete altitudes and to the near-surface rain rate, R. All of these TMI and PR data averaged to the 19 GHz *fov* are referred to from hereafter as *pixel* data.

The PR data show that rain rate can be highly variable within a 19 GHz *fov*. There can be 17 PR footprints of 4.3 km x 4.3 km in this *fov*. These 17 footprints can be sorted according to the PR classification as having no rain, stratiform rain, or convective rain. Here we assume PR-observed, near-surface rain rate is zero when it is less than 0.1 mmhr^{-1}. In this study, a given *pixel* is categorized as convective when 55 % or more of its area is covered by rain of convective type. This threshold of 55% is chosen because convective rain area tends to have a small scale. Similarly, a *pixel* is categorized as stratiform when 90 % or more of its area is covered by stratiform type of rain. Each one of these relatively pure convective and stratiform rain *pixels* is generally found to contain a small rain-free area. Of the total number of rain *pixels* in a given MCS, only about 15 % meet these strict criteria of convective and stratiform type. For the purpose of generating a set of TMI and PR data associated with such convective and stratiform *pixels*, we have utilized 20 MCS rain events observed by the TRMM satellite over diverse land regions of the tropics. The time, location, and the number of convective and stratiform *pixels* for each MCS case is presented in Table 1. Note, in order to reduce contamination from wet land surfaces, the data where the polarization difference between the vertical and horizontal channels in the 19 GHz is greater than 5 K are eliminated.
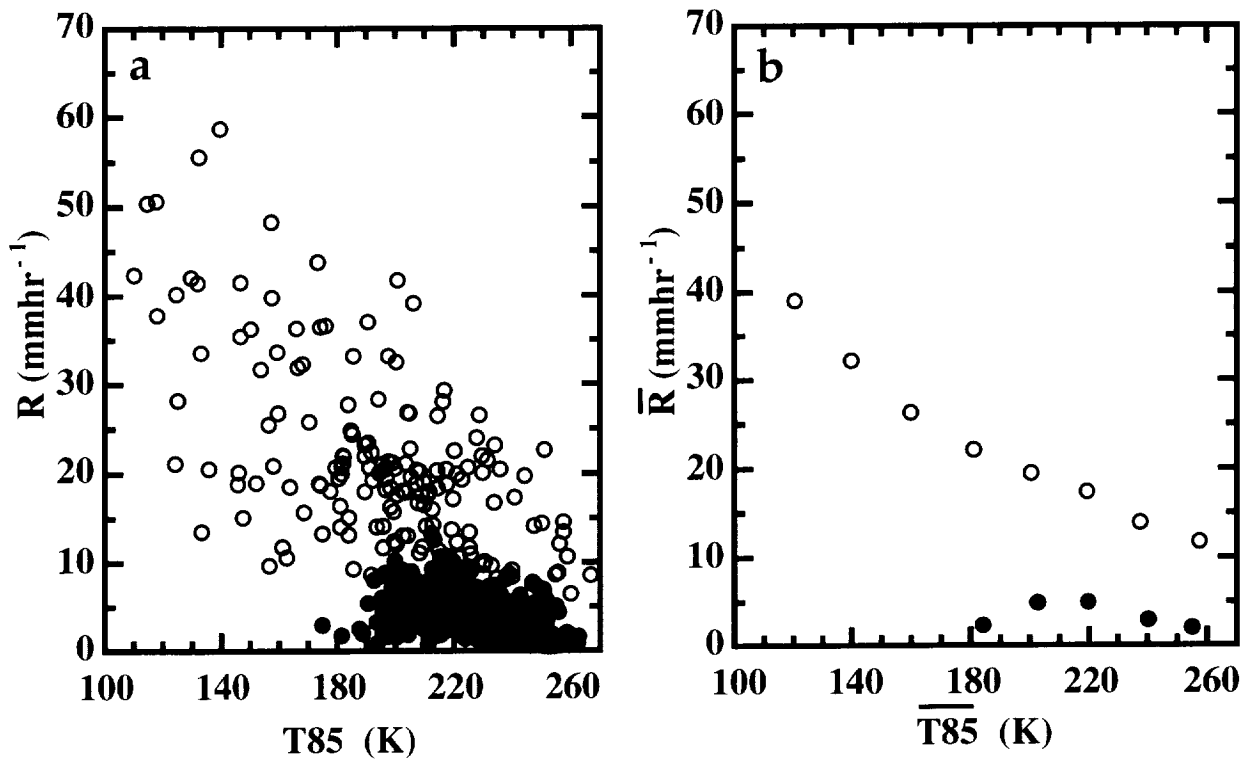
Figure 3: Observed PR rain rate versus 85 GHz brightness temperature for **a)** 20 km *pixels* and **b)** averages of 20 km *pixels* over 20 K intervals of T85. The open circles denote observations from convective regions, while the filled circles represent observations from stratiform regions. Data for these plots are taken from TRMM observations of 20 MCS cases over land.

In Figure 3a, we present a plot of T85 and the corresponding PR rain rate that have been averaged to the *pixel* scale. This data is gathered from the 20 MCS events listed in Table 1. From this plot, we see that the *pixels* characterized as convective by the PR have relatively high rain rates and the *pixels* characterized as stratiform have generally low rain rates. There is a lot of scatter in the data, however, generally T85 decreases as R increases. A closer examination of the PR data shows that most of the convective *pixels* have rain rates greater than 10 mmhr^{-1}, even at warm brightness temperatures as high as 260 K. In the stratiform *pixels*, more than 97 % have rain rates less than 10 mmhr^{-1}. Also, we find from Fig. 3a that the magnitude of the slope dT85/dR given by linear regression for convective rain is significantly smaller than that for stratiform rain. This observation suggests that T85 has more sensitivity to hydrometeors associated with stratiform rain. We may note that stratiform rain rate does not show a simple linear behavior with respect to T85.

To enhance further statistical strength in the *pixel* data described above, we have performed additional averaging. First the PR and TMI *pixel* data are sorted according to the T85 value. Then in each 20 K interval of T85, the TMI *pixel* data of T19, T37, and T85 are averaged. Similarly, the near surface rain rate given by PR and the reflectivity, Z, at individual altitudes are averaged. This has been done separately for convective and stratiform regions using the data from the 20 MCS events listed in Table 1. These averages of *pixels* are presented in Tables 2a and 2b. An overbar is used to denote these averages of *pixels* , i.e., $\overline{T19}$, $\overline{T37}$, $\overline{T85}$, $\overline{Z}$ and $\overline{R}$. Each row in these tables represents a sequential 20 K interval in T85 and is identified alphabetically. The number of *pixels* that are averaged in each row is also shown in the tables. It may be pointed out that the standard deviation of all observations of Z at each altitude for a given T85 interval of 20

14

Table 2: Average of PR and TMI 20 km pixel observations within a given 20 K interval of T85 for **a)** convective and **b)** stratiform rain. The averages are calculated for the following parameters: T85; T37; T19; convective rain fraction; PR near-surface rain rate, R; and PR reflectivity, Z, at 1, 3, 4, 4.5, 6, 7, 9, and 11 km. The number of 20 km pixel observations in a given T85 interval is also shown in these tables. Note, in the stratiform pixel statistics, the stratiform rain fraction is indicated instead of the convective rain fraction. The population of pixels used to generate these statistics associated with convective and stratiform rain is deduced from 20 MCS cases over land regions.

a) Convective Rain Pixel Statistics

	T85 Interval K	# of Pixs.	$\overline{T85}$ K	$\overline{T37}$ K	$\overline{T19}$ K	C %	S %	$\overline{R}$ $\frac{mm}{hr}$	$\overline{Z}$@ 1 km	$\overline{Z}$@ 3 km	$\overline{Z}$@ 4 km	$\overline{Z}$@ 4.5 km	$\overline{Z}$@ 6 km	$\overline{Z}$@ 7 km	$\overline{Z}$@ 9 km	$\overline{Z}$@ 11 km
A	110-130	8	120.4	202.8	258.5	72	24	39.1	1.0E5	1.3E5	1.0E5	7.7E4	2.2E4	9.7E3	2.7E3	9.9E2
B	130-150	11	139.8	210.6	258.4	72	24	32.2	9.8E4	1.1E5	8.4E4	6.1E4	2.0E4	1.1E4	2.7E3	8.5E2
C	150-170	17	159.8	224.3	263.4	71	25	26.4	6.4E4	6.5E4	4.4E4	3.1E4	9.4E3	4.3E3	1.1E3	3.8E2
D	170-190	27	180.9	242.8	269.5	70	23	22.2	4.8E4	3.5E4	2.3E4	1.7E4	4.8E3	2.3E3	4.7E2	2.1E2
E	190-210	49	200.1	251.1	272.2	69	22	19.5	3.0E4	2.3E4	1.6E4	1.2E4	2.8E3	1.3E3	3.8E2	1.2E2
F	210-230	32	219.2	257.5	273.9	67	24	17.4	2.4E4	1.6E4	1.2E4	8.3E3	1.6E3	4.6E2	1.0E2	7.5E1
G	230-250	14	237.5	263.6	276.7	61	24	14.0	2.0E4	1.3E4	1.1E4	1.0E4	2.5E3	7.6E2	2.1E2	1.0E2
H	250-270	9	257.4	269.6	277.1	58	28	11.8	1.5E4	8.5E3	6.7E3	5.8E3	1.9E3	6.6E2	1.5E2	1.2E1

b) Stratiform Rain Pixel Statistics

	T85 Interval K	# of Pixs.	$\overline{T85}$ K	$\overline{T37}$ K	$\overline{T19}$ K	C %	S %	$\overline{R}$ $\frac{mm}{hr}$	$\overline{Z}$@ 1 km	$\overline{Z}$@ 3 km	$\overline{Z}$@ 4 km	$\overline{Z}$@ 4.5 km	$\overline{Z}$@ 6 km	$\overline{Z}$@ 7 km	$\overline{Z}$@ 9 km	$\overline{Z}$@ 11 km
A	170-190	5	184.2	257.2	276.1	02	91	2.3	1.5E3	1.8E3	1.8E3	6.8E2	2.8E2	2.1E2	1.1E2	6.6E1
B	190-210	82	202.5	255.9	273.7	04	93	4.9	3.6E3	4.4E3	5.4E3	2.2E3	2.5E2	1.7E2	7.8E1	1.9E1
C	210-230	147	219.7	258.4	275.7	04	95	5.0	4.1E3	4.0E3	6.5E3	4.0E3	2.6E2	1.5E2	5.8E1	1.4E1
D	230-250	164	240.2	264.2	277.8	02	94	2.9	1.9E3	1.7E3	3.1E3	2.4E3	1.2E2	7.3E1	2.0E1	1.3E0
E	250-270	43	254.9	269.0	278.3	01	93	2.0	1.2E3	7.9E2	1.1E3	1.2E3	7.8E1	4.4E1	6.0E0	0.1E0

K has a magnitude that is comparable to the mean value itself. For each row in Tables 2a and 2b, the fractional area of convective rain (C) and stratiform rain (S) is indicated as a percentage. Also, since these two rain areas do not add up to 100 %, we can infer the rain-free area.

Taking the *pixel* averages given in Tables 2a and 2b, we present in Figure 3b the relationship between $\overline{R}$ and $\overline{T85}$ for the convective and stratiform regions. This figure shows clearly that when one averages the data in the above manner, the variability in the data is reduced, and a clear relationship between $\overline{R}$ and $\overline{T85}$ emerges. The convective rain rate increases non-linearly as $\overline{T85}$ decreases. This non-linear relationship resembles that derived from radiative transfer theory, where scattering from ice hydrometeors above the freezing level is included (see Wu and Weinman, 1984). The stratiform $\overline{R}$ increases slowly until $\overline{T85}$ decreases to 220 K, due to ice scattering. But, contrary to theoretical expectations, as $\overline{T85}$ decreases further, stratiform $\overline{R}$ also decreases. Thus, a different explanation is needed to understand this feature.

In Figures 4a and 4b, we present plots of $\overline{Z}$ at different altitudes in the atmosphere as a function of $\overline{T85}$ using the average *pixel* data given in Tables 2a and 2b. From Fig. 4a, we find that as $\overline{T85}$ increases from 120 K to 220 K, $\log_{10}\overline{Z}$ decreases almost linearly. However, when $\overline{T85}$ is near 240 K and 260 K, this linear trend is broken. In Fig. 4b, where the averages of the *pixel* data for the stratiform rain are presented, we find again that as $\overline{T85}$ increases from about 220 K to 260 K, $\log_{10}\overline{Z}$ decreases almost linearly. On the other hand, when $\overline{T85}$ is near 200 K and 180 K, this
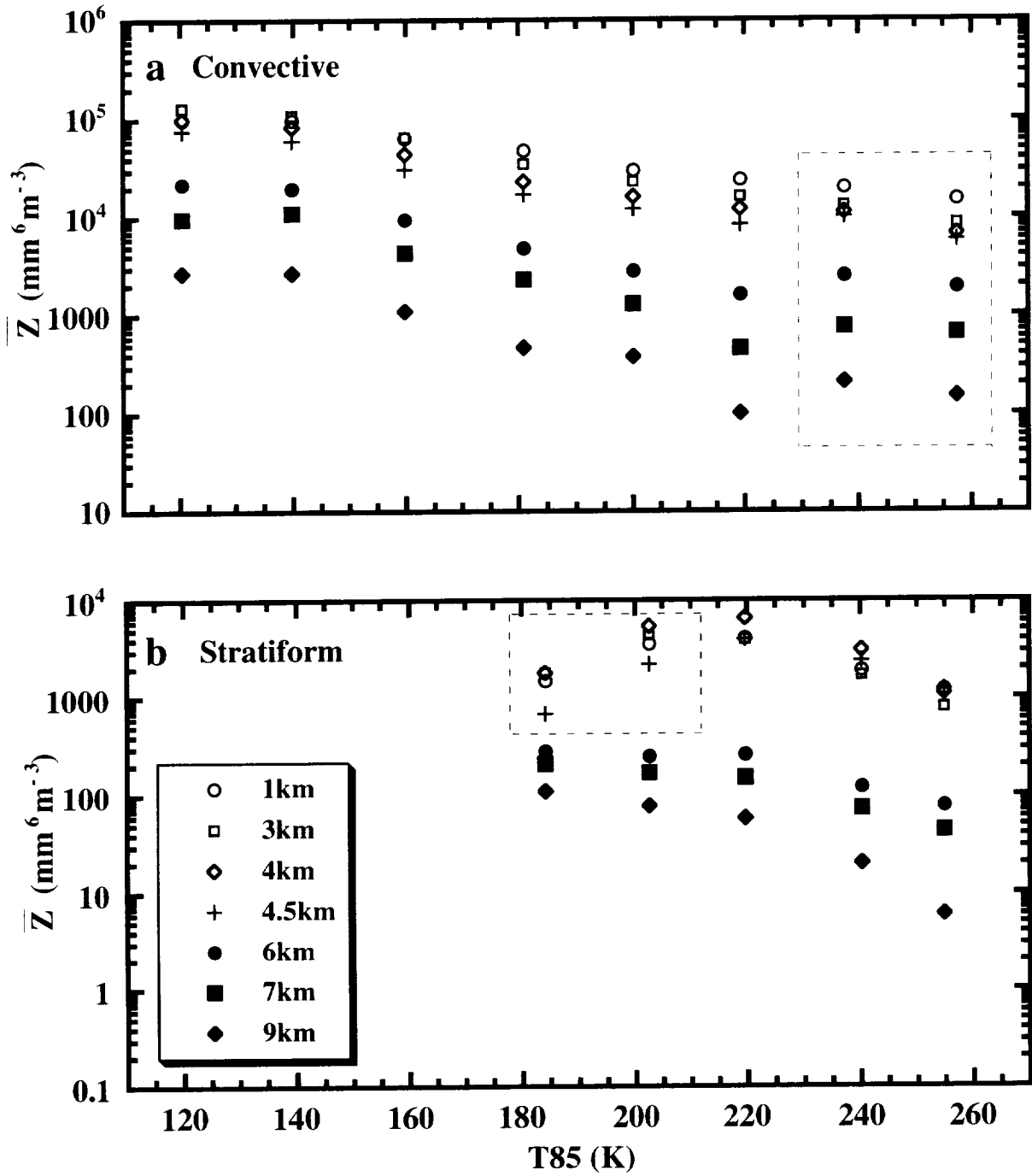
16

Figure 4: PR reflectivity, Z, at different altitudes versus $\overline{\text{T85}}$ for **a)** convective and **b)** stratiform rain. The symbols denoting the various altitudes are shown as an inset in Panel b. Also, the dashed boxes in both figures indicate data with pronounced anomalous character arising from differences of the viewing geometry of the TMI and PR observations.

trend in $\log_{10} \overline{Z}$ is again broken. Note, in the stratiform rain areas that the magnitude of $\overline{Z}$ in the reflectivity profiles decreases below the melting layer. This decrease can be noticed all the way to the surface in Rows A and B of Table 2b. This decrease is apparently due to evaporation of rain drops below the freezing level. The cause of the breakdown mention above in the relationship between $\overline{T85}$ and $\log_{10} \overline{Z}$ in convective and stratiform observations is possibly due to problems associated with the differences in viewing geometry of the TMI and PR, which cannot be totally eliminated by averaging. A good example that reveals the problems associated with differences in viewing geometry is shown schematically in Figures 5a and 5b when TMI and PR are viewing along the sub-satellite track.

In Fig. 5a, the BWER indicated within the anvil has weak stratiform rain near surface. A possible viewing geometry of PR and TMI with respect to the BWER is also illustrated in the figure. Based on this viewing geometry, we can infer that while the PR senses weak near-surface rain rate, the radiometer with an oblique view senses substantial reflectivity of ice hydrometeors aloft, which is typical in convective rain. In Fig. 5b, we show that the view of the PR is directly above the convective area, where the reflectivity is high. The conical view of the TMI on the other hand, is passing through low reflectivity layers aloft, before it views the same area at the surface. These combinations of radar and radiometer measurements shown in Fig. 5a for stratiform regions and Fig. 5b for convective regions lead to spurious information about rain in the TMI measurements. Also, from these illustrations, a possible explanation is given for the anomalous relationship between $\overline{T85}$ and $\log_{10} \overline{Z}$ discussed above. Furthermore, they could be used to explain relatively large convective rain rate
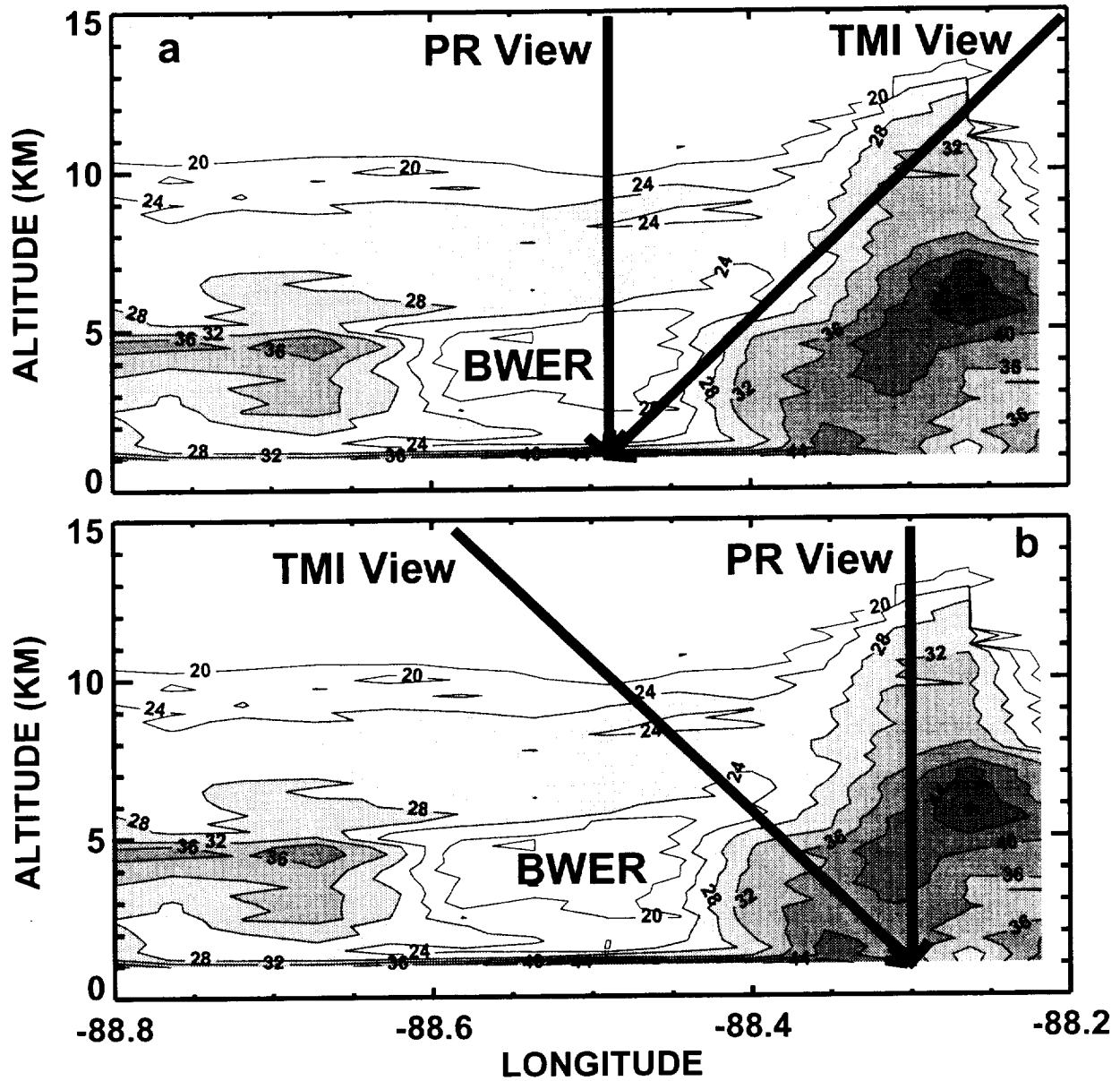
18

Figure 5: Possible viewing geometry of the PR and TMI in the vertical cross section shown in Figure 2a for the following *pixels*: **a)** a surface *pixel* underneath the Bounded Weak Echo Region (BWER), where the rain rate is weak and **b)** a surface *pixel* underneath a convective tower, where the rain rate is heavy.

($\sim$10 mmhr^{-1}) when T85 is warm ($>$ 240 K), and significantly small stratiform rain rate ($<$ 4 mmhr^{-1}) when T85 is cold ($<$ 220 K) as shown in Fig. 3b. Although we have used the example of BWER to explain strong anomalies, we expect that there will be anomalies in PR and TMI data whenever a vertical profile of Z is perturbed by differential horizontal advection, or other processes.

In convective rain, despite some problems due to viewing geometry, the PR and TMI observations shown in Fig. 4a demonstrate that there is a relatively strong relationship between $\overline{T85}$ and the vertical profiles of $\overline{Z}$. The brightness temperatures $\overline{T19}$ and $\overline{T37}$ have a weaker relationship with the radar reflectivity as shown in Table 2a. From this table, we note that the range in value of $\overline{T85}$, $\overline{T37}$ and $\overline{T19}$ from Row A to Row H is about 137 K, 67 K, and 18 K, respectively. The corresponding range in $\overline{R}$ is about 28 mmhr^{-1}. In addition, the rain rate and Tbs in all three channels vary systematically from Row A to Row H, with no minimum or maximum in between. On the other hand, from Table 2b we observe that such a systematic nature is missing in stratiform regions. The rain rate has a maximum value of 5 mmhr^{-1} where $\overline{T85}$ is about 220 K (see Row C in Table 2b). Also, $\overline{T37}$ and $\overline{T19}$ indicate a minimum in Row B. We believe the errors introduced by viewing geometry of TMI and PR in the weak stratiform rain regime are responsible for these anomalies.

Based on the averages of the *pixels* presented in Tables 2a and 2b, we note that for a given set of brightness temperatures - i.e., $\overline{T19}$, $\overline{T37}$ and $\overline{T85}$ - one can get widely different rain rates depending on the type of rain that is being observed. An example of this can be found by comparing the data in Row F in Table 2a and Row C in Table 2b.

From these rows, $\overline{T85}$ is close to 220 K, while $\overline{T37}$ and $\overline{T19}$ are close to 258 K and 275 K, respectively. However, we find near-surface rain rate, $\overline{R}$, deduced from PR for the convective rain is 17.4 mmhr^{-1}, while it is 5.0 mmhr^{-1} for the stratiform rain. This implies that the radiometer data are on the average insensitive to the type of rain. Thus, in order to estimate rain rate satisfactorily from TMI, it is critical to specify the nature of rain.

3. **Hydrometeor Profiles Applicable to Convective/Stratiform Radiative Transfer Models**

In order to simulate the observed characteristics of the Tbs in the 19, 37, and 85 GHz TMI channels, we have developed separate radiative transfer models applicable to convective and stratiform rain regions. The radiative transfer equation pertaining to these models includes absorption, emission, and scattering due to gases, cloud water, and liquid and frozen hydrometeors in the atmosphere. This equation, along with relevant boundary conditions, is presented in the Appendix. Also, a description of the procedure that we have adopted to estimate the extinction coefficients, single scattering albedos, and phase functions is presented in the Appendix.

In this section, we develop models of the hydrometeor profiles applicable to convective and stratiform rain regions that are used in our radiative transfer calculations. For this purpose, we utilize information from the reflectivity profile of PR, as well as results of studies based on polarimetric radar data. In addition, particle size distribution information from past analyses of aircraft observations made by several investigators is incorporated.

3.A. General Considerations

The basic strategy that we have implemented for both the convective and stratiform models is to simulate the brightness temperatures T85, T37, and T19 for each profile of reflectivity, $\overline{Z}$, given in Tables 2a and 2b. Then, these simulated Tbs are compared with the observed $\overline{T85}$, $\overline{T37}$, and $\overline{T19}$ to establish the physical relationship between the TMI and PR measurements. In our models, the radar reflectivity is given by

$$\overline{Z} = C\int D^6 N(D)dD, \tag{1}$$

where $N(D)$ [m^{-4}] is the number density of particles in a given size range dD [m], and D [m] is the particle diameter. In the case of snow or graupel, the particle diameter is represented by the equivalent melted diameter (see Ulaby et al., 1981). The constant C, which depends on the refractive index, differs between water and ice particles. For water, C has a value of 1.0, while C is 0.19/0.93 for ice. The particle size distribution (PSD) is described using the Marshall-Palmer size distribution, as given below:

$$N(D) = N_o \exp(-\lambda D). \tag{2}$$

In this equation, N_0 [m^{-4}] and λ [m^{-1}] are the intercept and slope parameters of the PSD. In order to match $\overline{Z}$ measured by PR, N_0 is given a value based on observations, such as those of Houze et al. (1979) and Sekhon and Srivastava (1970). Then, an appropriate value of λ is determined with an iterative procedure that utilizes Equations 1 and 2.

From Eq. 2, we can define the weighted-mean diameter, <D> [μm], of the PSD as

$$\langle D \rangle = 10^6 \frac{\int N(D)DdD}{\int N(D)dD}.$$ (3)

Also, the equivalent water content, W [gm^{-3}], is given by

$$W = 10^6 \frac{\pi}{6} \rho_w \int N(D)D^3 dD,$$ (4)

where ρ_w [g cm^{-3}] is the density of water. Furthermore, we can express the rain rate, R [mmhr^{-1}], in the following manner (see Bennarz and Petty, 2001)

$$R = 3.6 \times 10^6 \frac{\pi}{6} \int N(D)U(D)D^3 dD,$$ (5)

where U(D) [ms^{-1}] is the fall velocity of the rain drops as a function of drop diameter. Thus, for a given radar reflectivity, $\bar{Z}$, we note that R calculated from Eq. 5 is directly dependent upon N(D). In this study, we adopt the Marshall-Palmer PSD (Eq. 2). Therefore, the rain rate deduced from $\bar{Z}$ depends on the parameters N_0 and λ.

Since the nature of the hydrometeor profile is different in the convective and stratiform regions, the radiative transfer models applicable to these two regions differ. In the next section details pertaining to these models are elaborated.

3.B. Convective Model

In our convective model, the surface temperature over tropical land is set at 302 K, and the temperature lapse rate is 6.0 Kkm^{-1}. This gives a freezing level close to 5.0 km. The water vapor distribution in this atmosphere is taken such that the relative humidity is 80 % between the surface and cloud base, and 100 % above. The cloud base is set at 1.5 km, and the cloud liquid water content below the freezing level is assumed to increase linearly from 0.5 gm^{-3} to 1.0 gm^{-3} as surface rain rate increases from 2.0 mmhr^{-1} to 40.0 mmhr^{-1}.

The PSD at all model levels is inferred using a single value of N_0. Below the freezing level, all hydrometeors are assumed to be water drops. We have adopted a model of the hydrometeor profile above the freezing level. Observations of differential reflectivity (Z_{DR}) and linear depolarization ratio (LDR) made by polarimetric radars (Smith et al., 1999; Bringi et al., 1997; Balakrishnan and Zrnic, 1990; and Sax and Keller, 1980) are used in developing this model. These measurements of Z_{DR} and LDR lead to an inference of a layer of mixed-phase particles, consisting of water and ice, to a substantial height above the freezing level, because of vigorous vertical motions in convective updrafts. The relatively strong reflectivity (> 30 dBZ) observed by PR in convective towers above the freezing level (see Fig. 2a) also supports this inference. The detailed nature of these mixed-phase particles - i.e., the fraction and distribution of water and ice in them - is not considered in this study, because of insufficient information. For this reason, in our convective model, we assume for simplicity that there is a mixed layer of finite depth above the freezing level where water drops and frozen graupel exist together in some proportion. The density of water drops and

24

graupel are respectively 1.0 gcm^{-3} and 0.4 gcm^{-3}. The volume fractions of water drops (f_{wat}) and graupel (f_{ice}) at each level in the mixed layer are given as follows:

$$f_{ice} = \left(\frac{h - h_F}{H}\right)^{0.25} \quad \text{where} \quad h_F < h < h_T$$
$$f_{wat} = 1 - f_{ice}.$$

$$(6)$$

Here h_F is the height of the freezing level, and h is the height of any given level in the atmosphere. Now, if we denote the height of the top of the mixed layer as h_T, then the thickness H of the mixed layer is given by $H = h_T - h_F$. Equation 6 leads to 100 % liquid phase at the freezing level, which nonlinearly approaches 0 % as h tends to h_T. Above this mixed layer, we assume all hydrometeors are completely frozen graupel with a density of 0.4 gcm^{-3}.

Given N_0 and H, we can define the N(D) for the ice and water particles at each level based on the $\overline{Z}$ profile and Eqs. 1, 2 and 6. With this information, we can calculate the Mie volume absorption and scattering coefficients, k_a and k_s, as well as the phase function, **P**, as a function of height using the procedure developed by Wiscombe (1980). We may note these properties k_a, k_s and **P** depend on the real and imaginary parts of the refractive index of water and ice. For graupel the values of refractive index are computed as a function of the particle density, which depends on the volume fraction of air and ice (Liao and Meneghini, 2000). This information allows us to calculate Tbs at the top of the atmosphere for a particular viewing angle of the radiometer with the help of the radiative transfer equation and the boundary conditions also described in the Appendix. The computational procedure described above is utilized to simulate the

observed $\overline{T85}$, $\overline{T37}$, and $\overline{T19}$ with the $\overline{Z}$ profile given in each row (see Table 2a) and for each combination of N_0 and H.

In summary, the procedure discussed above amounts to calculating Tbs using a hydrometeor profile that is consistent with the profiles of $\overline{Z}$. Implicitly this profile of hydrometeors depends on the prescribed values of N_0 and H.

3.C. Stratiform Model

In the stratiform model, the vertical profile of temperature is the same as that in the convective model. The water vapor distribution in this atmosphere is taken such that the relative humidity is 80 % between the surface and the freezing level, and 100 % above. At altitudes above the freezing level (~5.0 km), only ice aggregates (snow flakes) are assumed to exist. The density of ice aggregates, ρ_{ice}, is given as follows:

$$\rho_{ice} = \frac{2.0}{D_{sn}^{2}},$$

(7)

where D_{sn} [mm] is the diameter of a spherical particle whose volume is equal to the volume of the ice aggregate. Equation 7 is based on a similar expression developed by Magono and Nakamura (1965) (see also Schols et al., 1999). In Eq. 7, the limiting value of ρ_{ice} is set equal to 0.7 gcm^{-3}, as was done by Schols et al.. For the stratiform simulations, we have developed a model for the shape parameter, N_0, of the PSD above the freezing level. This model is based on the observational studies of Houze et al. (1979) and Sekhon and Srivastava (1970). Houze et al. showed that N_0 increases as the atmospheric temperature decreases, while Sekhon and Srivastava revealed that in

26

the stratiform region N_0 decreases as water content in the atmosphere increases. Based on this information, we have developed an empirical equation to give N_0 as a function of height above the freezing level in the atmosphere as follows:

$$N_0(R,h) = N^* \exp\left\{ R^{-0.94} + (h - h_F) \right\}, \tag{8}$$

where $h-h_F$ is the height, in kilometers, above the freezing level and R is rain rate. In Equation 8, the argument of the exponential function is forced not to exceed a value of 3.0. Also, the value of N_0 is not allowed to exceed 3×10^8 m^{-4}. This maximum value of N_0 is consistent with the observations of Houze et al. (1979). Below the freezing level, N_0 is given as

$$N_0(R) = N^* \exp\left\{ R^{-0.94} \right\}. \tag{9}$$

The value of the parameter N^* in Eqs. 8 and 9 is varied over a range between 10^5 m^{-4} and 10^7 m^{-4} to evaluate the impact of this parameter on the upwelling brightness temperature.

In our stratiform model, we have a layer of relatively-large, slowly-falling, low-density, melting snow flakes below the freezing level. The depth of the melting layer is taken to be 500 m. To estimate the refractive index of these melting snow flakes, we have adopted the Maxwell-Garnet mixing model of ellipsoidal ice inclusions randomly distributed in a homogeneous water matrix (Meneghini and Liao, 1996 and 2000). In this combination, the water contribution dominates for all meltwater fractions (Bauer et al., 2000). In our stratiform model, it is assumed that these snow flakes melt completely and form raindrops at the base of the melting layer.

The hydrometeor profiles described above for the stratiform rain model are constructed to be consistent with the stratiform profiles of $\overline{Z}$ given in Table 2b. As in the convective model, we compute the Mie volume extinction and scattering coefficients, as well as the phase function, as a function of height for these hydrometeor profiles. This information is used to calculate Tbs at the top of the atmosphere for a particular viewing angle of the radiometer with the help of the radiative transfer equation and the boundary conditions presented in the Appendix. From the description of the hydrometeor profile, we note that N^* is the key parameter for the stratiform region.

4. Results and Discussion

For the purpose of this study, the sensitivity of Tbs in the convective model is examined with respect to the hydrometeor profile parameters N_0 and H. In the stratiform model, this sensitivity is examined with N^*. These results are given for convective and stratiform model simulations in Subsections 4.A and 4.B, respectively.

4.A. Simulations for Convective Rain Regions

In Figures 6a-c, we have plotted T85, simulated with the convective model, as a function of the observed $\overline{T85}$ given in each row of Table 2a. In each figure panel, we show three curves, which represent T85 simulated using three different values of H (1, 3, and 5 km). Furthermore, in order to show the dependence of these results on N_0, we present in three figure panels T85 simulated using three N_0 values (2.0×10^6, 2.0×10^7, and
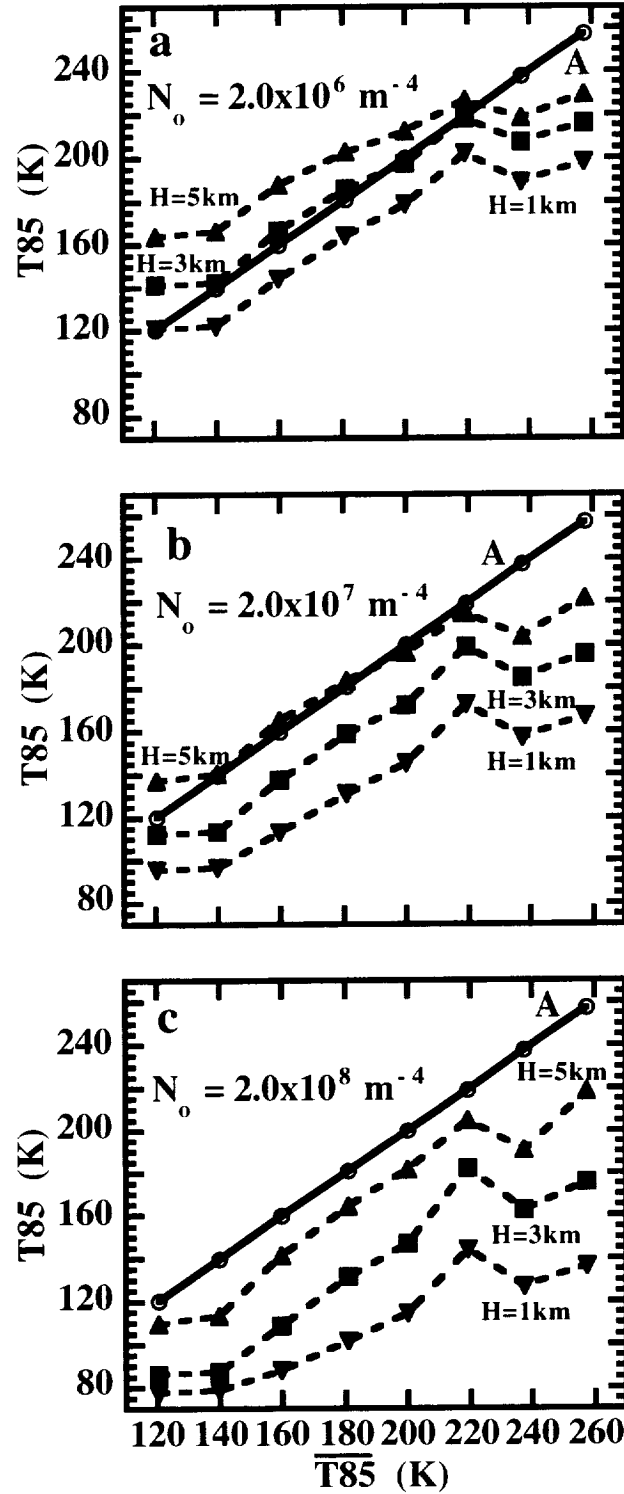
Figure 6: For the convective regions, dashed lines indicate simulated T85 versus observed $\overline{T85}$ for the following three values of N_0: **a)** 2×10^6 m^{-4}, **b)** 2×10^7 m^{-4}, and **c)** 2×10^8 m^{-4}. In each figure, the depth, H, of the mixed layer above the freezing level is indicated for each curve. The solid line **A** in these figures representing $\overline{T85}$ is included for comparison.

2.0×10^8 m^{-1}). To appreciate the effectiveness of these simulations, we also present in each one of these figure panels a curve showing the observed $\overline{T85}$, which is labeled curve **A**.

We find from Figs. 6a-c, that as the depth, H, of the mixed layer increases, the curves of simulated T85 tend to warmer values, because of reduced ice scattering. Varying N_0 also has an effect on the simulated T85 values. When N_0 is 2.0×10^8 m^{-1}, all three curves representing H equal to 1, 3, and 5 km are too cold with respect to curve **A**. As the parameter N_0 decreases, the simulated curves increase in temperature with respect to curve **A**. From the result given above (Figs. 6a-c), we conclude that by using the Marshall-Palmer representation of the PSD, suitable combinations of H and N_0 can be determined that can crudely explain the relationship between $\overline{T85}$ and the profiles of $\overline{Z}$. We observe that when N_0 is 2.0×10^6 m^{-1} and H is 3 km (Fig. 6b), the simulated T85 can explain the observed $\overline{T85}$ reasonably well. A significant point to note is that simulated T85 tends to underestimate observed $\overline{T85}$ values near 240 K and 260 K for all N_0 and H. This may be a consequence of the differences of the viewing geometry of PR and TMI, an example of which is shown in Fig. 5b. Note also that when N_0 is large, it leads to small weighted-mean diameter $\langle D \rangle$, and large water content, W (see Figures 9b and 9c).

In order to appreciate the sensitivity of T37 to H, we have computed T37 using the convective model for three values of H (1, 3, and 5 km) when N_0 is equal to 2×10^6 m^{-1}. These results are displayed with the three curves in Figure 7a. Here the observed $\overline{T85}$ given in Table 2a is used as the independent variable along the X axis. This helps to
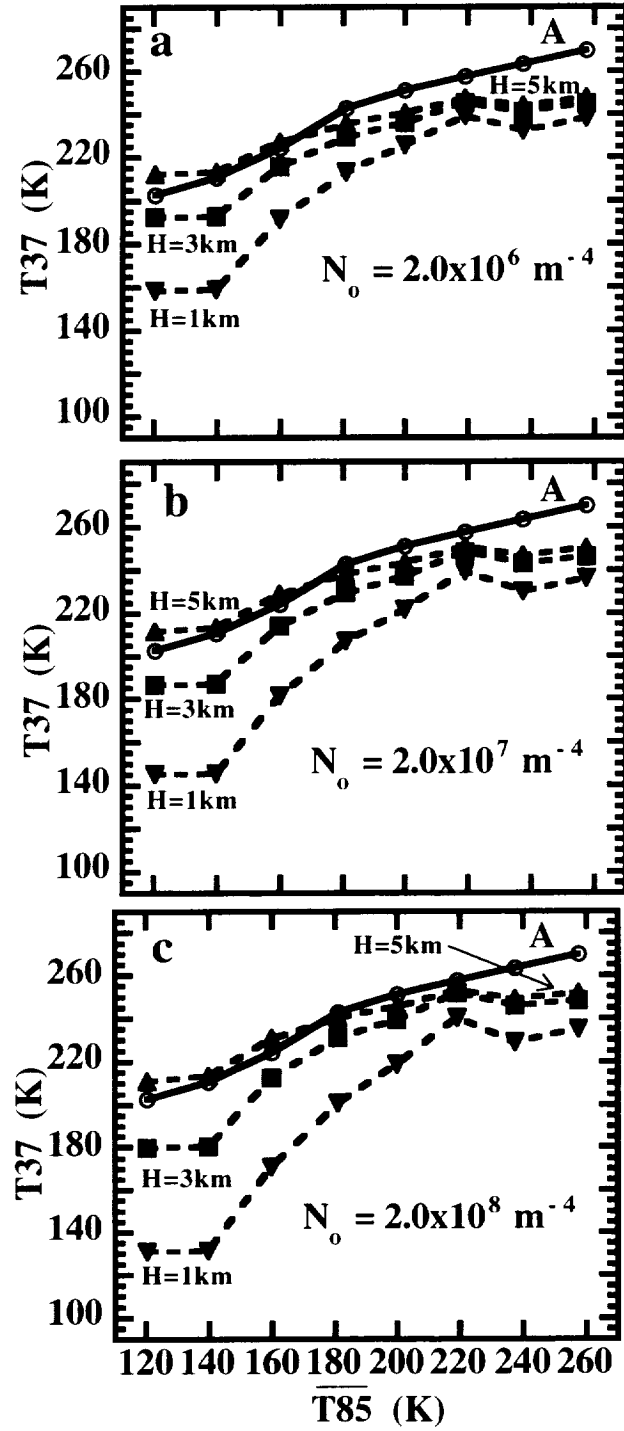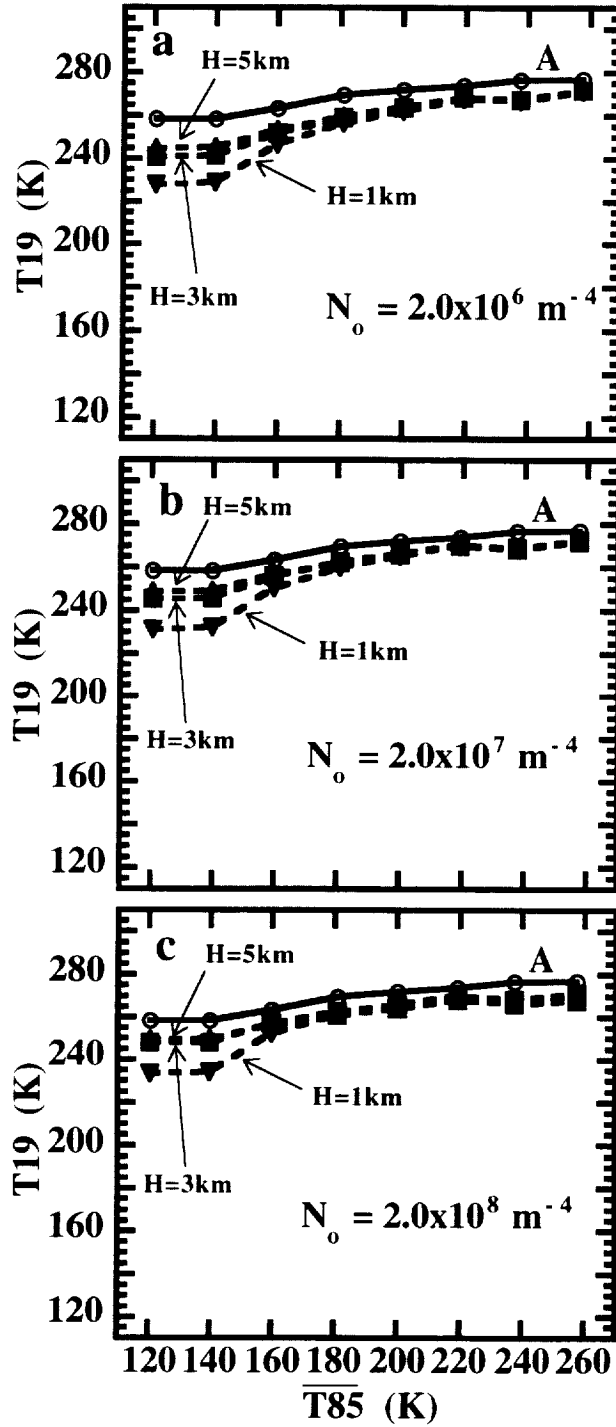
Figure 7: For the convective regions, dashed lines indicate simulated T37 versus observed $\overline{T85}$ for the following three values of N_0: **a)** 2×10^6 m^{-4}, **b)** 2×10^7 m^{-4}, and **c)** 2×10^8 m^{-4}. In each figure, the depth, H, of the mixed layer above the freezing level is indicated for each curve. The solid curve **A** in these figures representing $\overline{T37}$ is included for comparison.
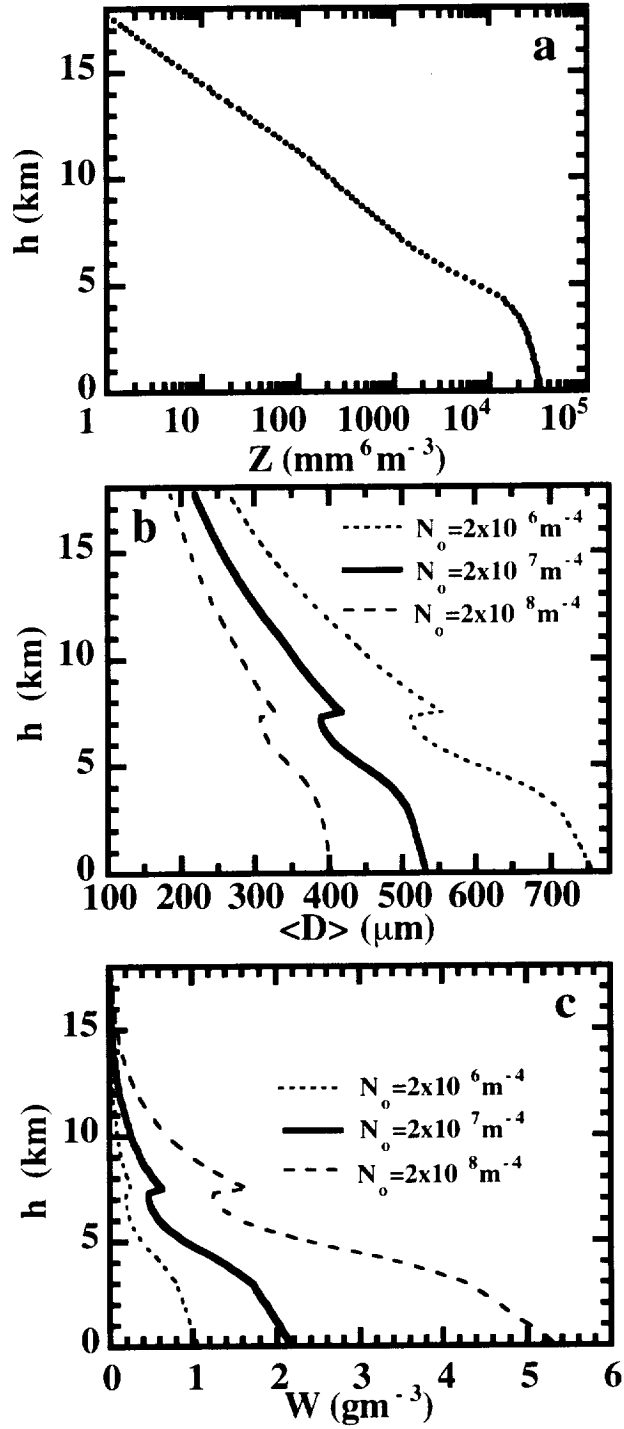
Figure 8: For the convective regions, dashed lines indicate simulated T19 versus observed $\overline{T85}$ for the following three values of N_0: **a)** 2×10^6 m^{-4}, **b)** 2×10^7 m^{-4}, and **c)** 2×10^8 m^{-4}. In each figure, the depth, H, of the mixed layer above the freezing level is indicated for each curve. The solid curve **A** in these figures representing $\overline{T19}$ is included for comparison.

Figure 9: Deduced from the data in Table 2a Row E, convective profiles of average **a)** reflectivity, $\bar{Z}$, **b)** weighted mean diameter of the PSD, <D>, and **c)** equivalent water content, W. The three curves in Panels b and c represent the sensitivity of <D> and W to the following N_0 values: 2×10^6, 2×10^7, and 2×10^8 m^{-4}. Also, the value of H is 3 km.

compare the information given in Fig. 7a with that of Fig. 6a. Similar results obtained from simulations using N_0 equal to 2×10^7 m^{-4} and 2×10^8 m^{-4} are presented respectively in Figures 7b and 7c, which can be compared with Figs. 6b and 6c. The curve **A** shown in Figs. 7a-c represents the observed $\overline{T37}$. This curve **A** is presented to evaluate the merits of the simulations of T37 obtained from the radiative transfer model. From these figures, we note that T37 is not as sensitive to N_0 as T85, because of the weak extinction to ice particles (see Figure 10b). We find $\overline{T37}$ is underestimated by about 5 to 10 K by the simulations when $\overline{T85}$ is greater than 180 K. Simulations similar to those of 85 GHz and 37 GHz are presented for the 19 GHz in Figures 8a-c. Also, from an examination of these figures, we find the simulated T19 is systematically colder than $\overline{T19}$ by about 10 to 15 K. These figures show a much reduced sensitivity to H and N_0.

As discussed earlier (Figs. 6a-c), we infer that the link between $\overline{T85}$ and $\overline{Z}$ can be explained in terms of suitable PSD and mixed-layer depth, H. On the other hand, simulations with the same PSD and H do not explain very well the link between observed $\overline{T37}$ and $\overline{Z}$, or the link between observed $\overline{T19}$ and $\overline{Z}$. For example, from an examination of the 19 GHz simulations (see Figs. 8a-c), we note again that the simulated T19 are systematically colder than the observed $\overline{T19}$. This may be due to the following reasons. Unlike the plane-parallel, vertically-stratified atmosphere assumed in the simulations, convective clouds are finite in size. Between these convective clouds there can be significant areas of non-raining clouds, which can be inferred from the percentage of convective and stratiform rain shown in Table 2a. An appreciable amount of radiation from the surface and lower layers of atmosphere can reach the radiometer through these non-raining clouds in 37 and 19 GHz channels. For example,

if a non-raining cloud has a thickness of 2 km with a cloud liquid water content of 0.5 gm^{-3}, we estimate the transmission to the surface in 85, 37, and 19 GHz is about 0.1, 0.45, and 0.8, respectively. Thus, the simulated values of T37 and T19, which are computed assuming horizontally-uniform rain area, can be colder than the observed values, since they do not take into account the contamination from the warm surface and lower atmosphere. When the difference T19-T37 obtained from simulations is considered, we find this difference correlates better with T85. This finding is in good agreement with the data shown in Figs. 1c and 1d.

In order to understand the various physical aspects of the radiative transfer leading to the results shown in Figs. 6, 7, and 8, we graphically present for one case the information that enters the convective simulations. In Figure 9a, the profile of $\overline{Z}$ in Table 2a when $\overline{T85}$ is equal to 200 K (Row E) is presented. For this profile of $\overline{Z}$, in Fig. 9b we show the vertical profiles of the weighted-mean diameter, <D>, of the PSD for the three different N_0 values, when H is equal to 3 km. The profiles of equivalent water content, W, for these conditions are shown in Fig. 9c. The associated profiles of the extinction coefficients are illustrated for the 85, 37 and 19 GHz in Figures 10a-c. From Fig. 9b, we show that for a given reflectivity, $\overline{Z}$, profile, the weighted-mean diameter (see Eq. 3) increases as N_0 decreases. Then, from Fig. 9c, we find that the corresponding equivalent water content, W, increases as N_0 increases. This relationship follows from Eqs. 1-4. Furthermore, increases in W are associated with increases in extinction in the 85, 37, and 85 GHz channels (see Figs. 10a-c). In Figure 11, the weighting function, $d\tau'/dh$, where τ' is the transmission of the atmosphere from the top to any given level h, is presented for all three radiometer channels. Here, the value of N_0 is 2×10^7 m^{-4} and H is equal to 3 km. Figure 11 illustrates that the longer wavelength channels at 37 and
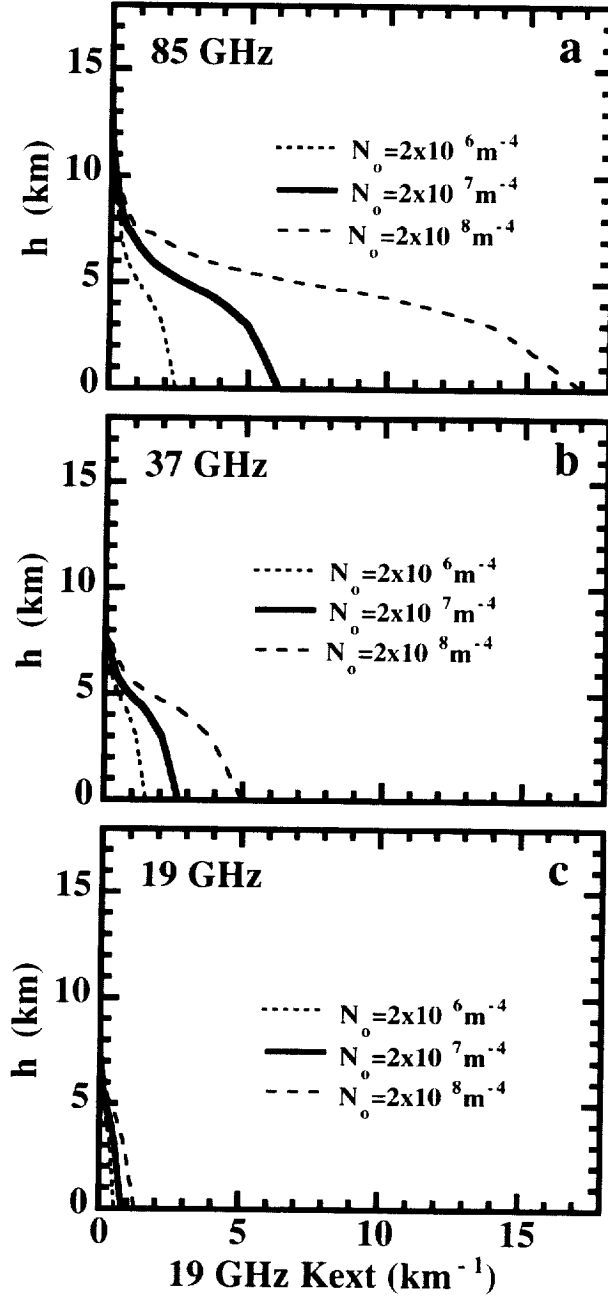
Figure 10: Extinction profiles for one convective region computed from Mie Theory for the **a)** 85 GHz, **b)** 37 GHz, and **c)** 19 GHz channels. Each extinction profile is deduced from the hydrometeor profile that is generated using $\overline{Z}$ (see text) given in Table 2a Row E. The three extinction profiles in each panel are produced by varying N_0 values: 2×10^6, 2×10^7, and 2×10^8 m^{-4}. Also, the value of H is 3 km.
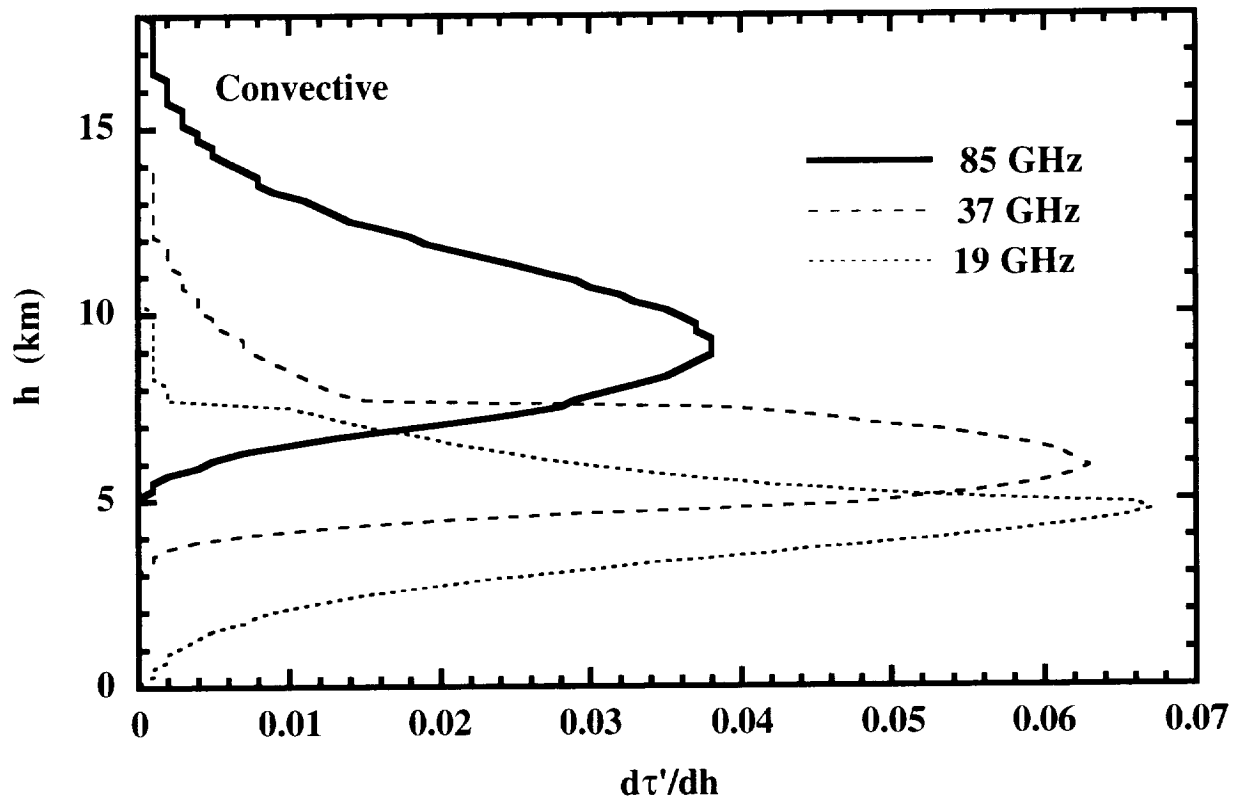
Figure 11: The weighting functions for the convective region for the 85 GHz (dark solid line), 37 GHz (dashed line), and 19 GHz (dotted line) channels. These weighting functions are derived using the $\overline{Z}$ profile in Table 2a Row E. Also, the parameters H and N_0 are 3 km and 2×10^7 m^{-4}, respectively.

19 GHz are more responsive to the lower regions of the atmosphere compared to the shorter wavelength 85 GHz channel.

4.B. Simulations for Stratiform Rain Regions

In Figures 12a-c, we are presenting the results obtained from the simulations pertaining to the stratiform observations presented in Table 2b. Three curves (dashed lines) shown in each one of these figure panels correspond to simulations based on three different values of N^* (10^5, 10^6, and 10^7 m^{-4}). In addition, a curve labeled **A** represents observed brightness temperatures. The 85 GHz simulations presented in Fig. 12a show that when N^* is 10^6 m^{-4}, a crude agreement between the observed $\overline{T85}$ and simulated T85 can be obtained, except when $\overline{T85}$ is near 180 K and 200 K. At these points, the $\overline{Z}$ data (see Table 2b Rows A and B) are most likely affected by the problems related to differences in the radar and radiometer viewing geometry (see Fig. 5a), and also possible evaporation below the freezing level.

We find from Fig. 12b, that when N^* is 10^6 m^{-4}, the simulated T37 agrees poorly with observed $\overline{T37}$. The simulated T37 shows a minimum when $\overline{T85}$ is equal to 220 K, which is not seen in the observations. We may remark that T37 is less sensitive to N^* than simulated T85. From an examination of Fig. 12c, we note the problems present in the simulation of T37 are compounded further in the T19 simulations.

In order to understand the various physical aspects of the radiative transfer leading to the results shown in Fig. 12, we graphically present information that is relevant to the stratiform simulations. This information corresponds to the profile of $\overline{Z}$
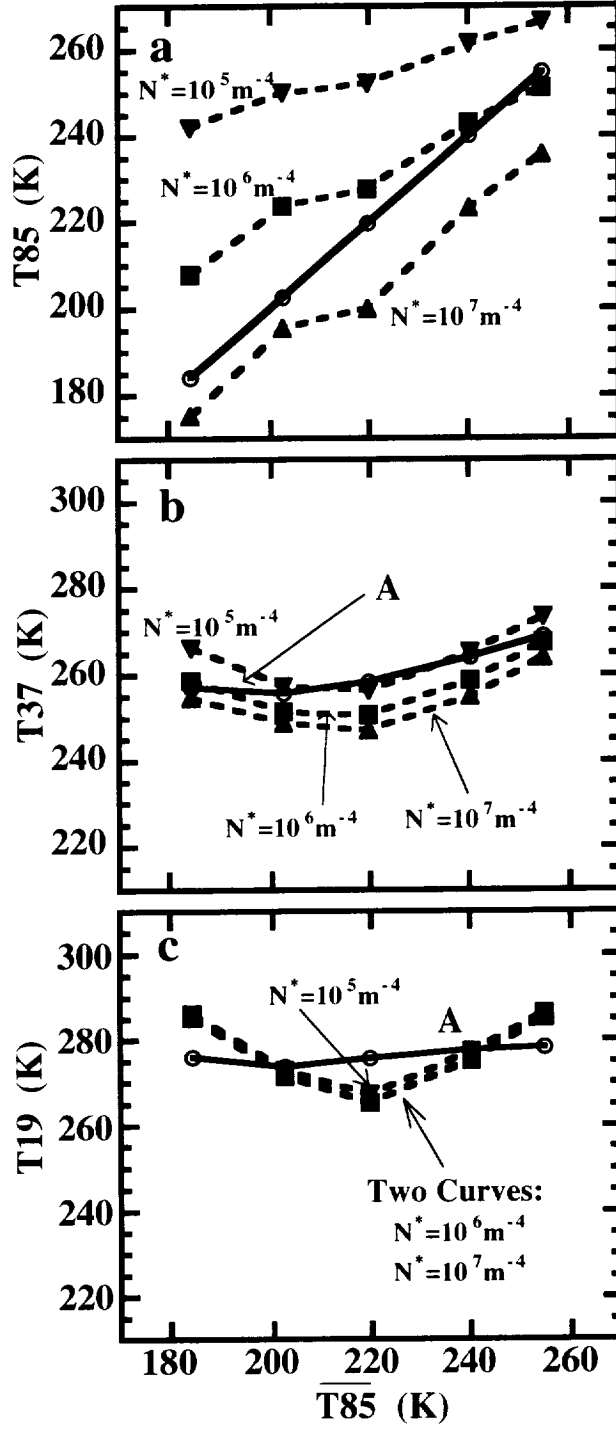
Figure 12: For the stratiform regions, dashed lines indicate simulated **a)** T85, **b)** T37, and **c)** T19 versus observed $\overline{T85}$ for the following three values of N^*: 10^5, 10^6, and 10^7 m^{-4}. For comparison, the solid line **A** representing the observations $\overline{T85}$, $\overline{T37}$, and $\overline{T19}$ are presented in Panels a, b, and c , respectively.
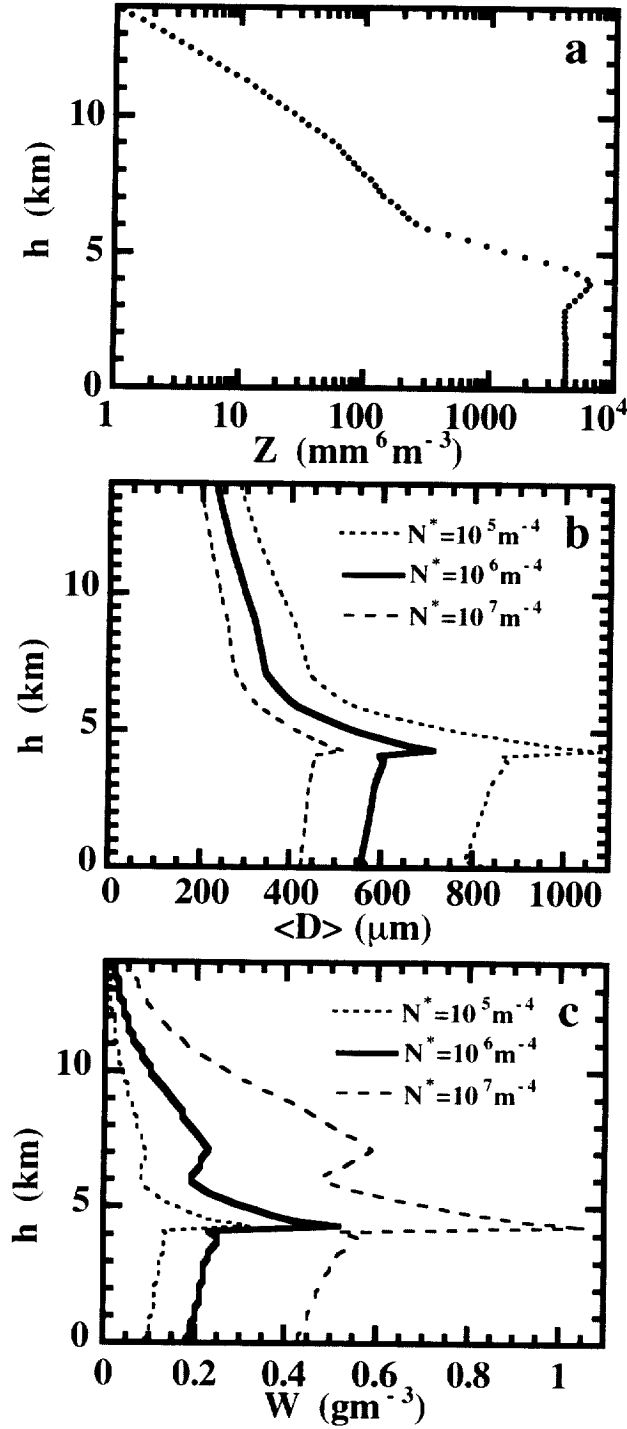
Figure 13: Profiles of a) reflectivity, b) weighted mean diameter of the PSD, and c) equivalent water content for the average of stratiform rain pixels given in Table 2b Row C. The three curves in Panels b and c represent the sensitivity of <D> and W to the following N^* values: 10^5, 10^6, and 10^7 m^{-4}.

in Row C of Table 2b when $\overline{T85}$ is equal to 220 K (see Figure 13a). In Figure 13b, we show the vertical profiles of the weighted-mean diameter, <D>, of the PSD for the three different N^* values. The profiles of equivalent water content, W, corresponding to these conditions are shown in Figure 13c. The related profiles of the extinction coefficients are illustrated for the 85, 37 and 19 GHz in Figures 14a-c. In a gross fashion, these extinction profiles are similar to the profiles of the water content presented in Fig. 13c. The weighting function, $d\tau'/dh$, where τ' is the transmission of the atmosphere from the top to any given level h, is presented for all these channels in Figure 15. Here, the value of N^* is 10^6 m^{-4}. These weighting functions clearly show the significance of the bright band, particularly in the 37 and 19 GHz channels. The strength of the bright band depends significantly on N^*.

From the analysis presented above, we infer that the crude agreement obtained in the 85 GHz channel between the observations and simulations when N^* is 10^6 m^{-4} is a consequence of the radar reflectivity profile above the freezing level (~5.0 km). This profile above the freezing level shows a decrease in $\overline{Z}$ (see Table 2b) as the observed $\overline{T85}$ increases (see also Fig. 4b). As a result, this crude agreement is produced in the 85 GHz channel. Such an agreement is not obtained when N^* is 10^6 m^{-4} between the 37 and 19 GHz observations and simulations. Simulated T37 and T19 show a minimum when $\overline{T85}$ is equal to 220 K, while the observed $\overline{T37}$ and $\overline{T19}$ do not (see Figs. 12b and 12c). A reason for this minimum in simulated T37 and T19 can be given as follows. From Table 2b, we discern that the reflectivity below the freezing level in Row C, where $\overline{T85}$ is equal to 220 K, is the largest of all the rows. This implies absorption due to rain below the freezing level is also the largest of all the rows. This accounts for the minimum in the simulated T37 and T19. Thus, we infer the disagreement between the
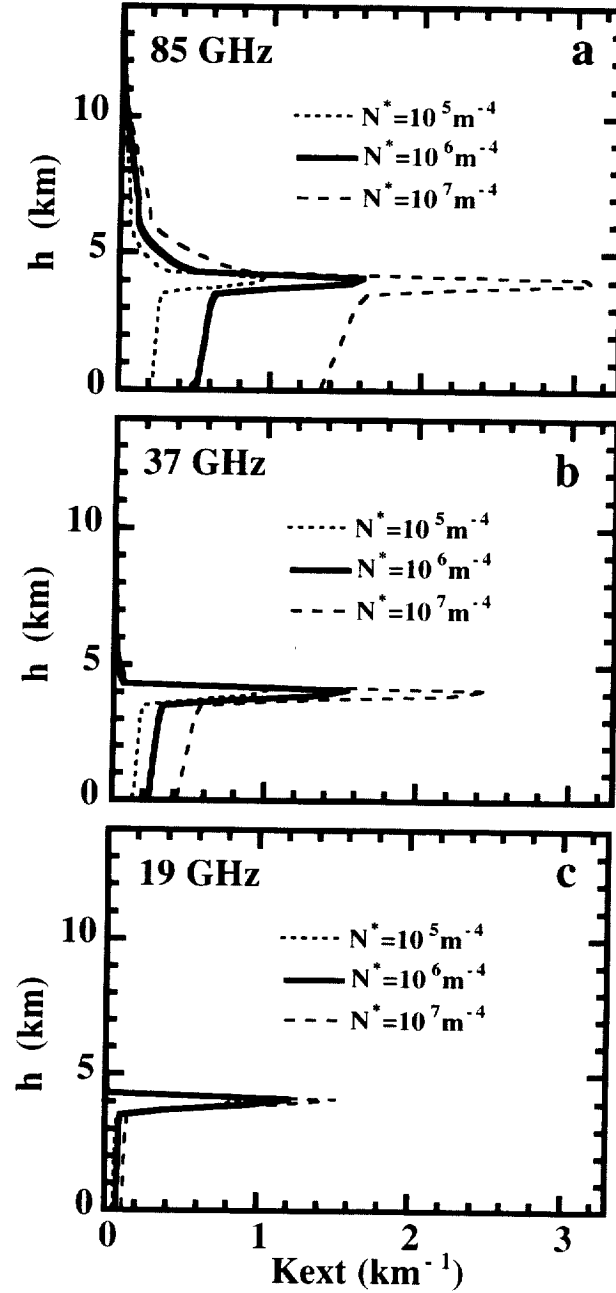
Figure 14: Stratiform extinction profiles computed from Mie Theory for the **a)** 85 GHz, **b)** 37 GHz, and **c)** 19 GHz channels. Each extinction profile is deduced from the hydrometeor profile that is generated using $\overline{Z}$ from PR given in Table 2b Row C and a Marshall-Palmer PSD. The three curves in each panel represent the sensitivity of the extinction profiles to the following N^* values: 10^5, 10^6, and 10^7 m^{-4}.
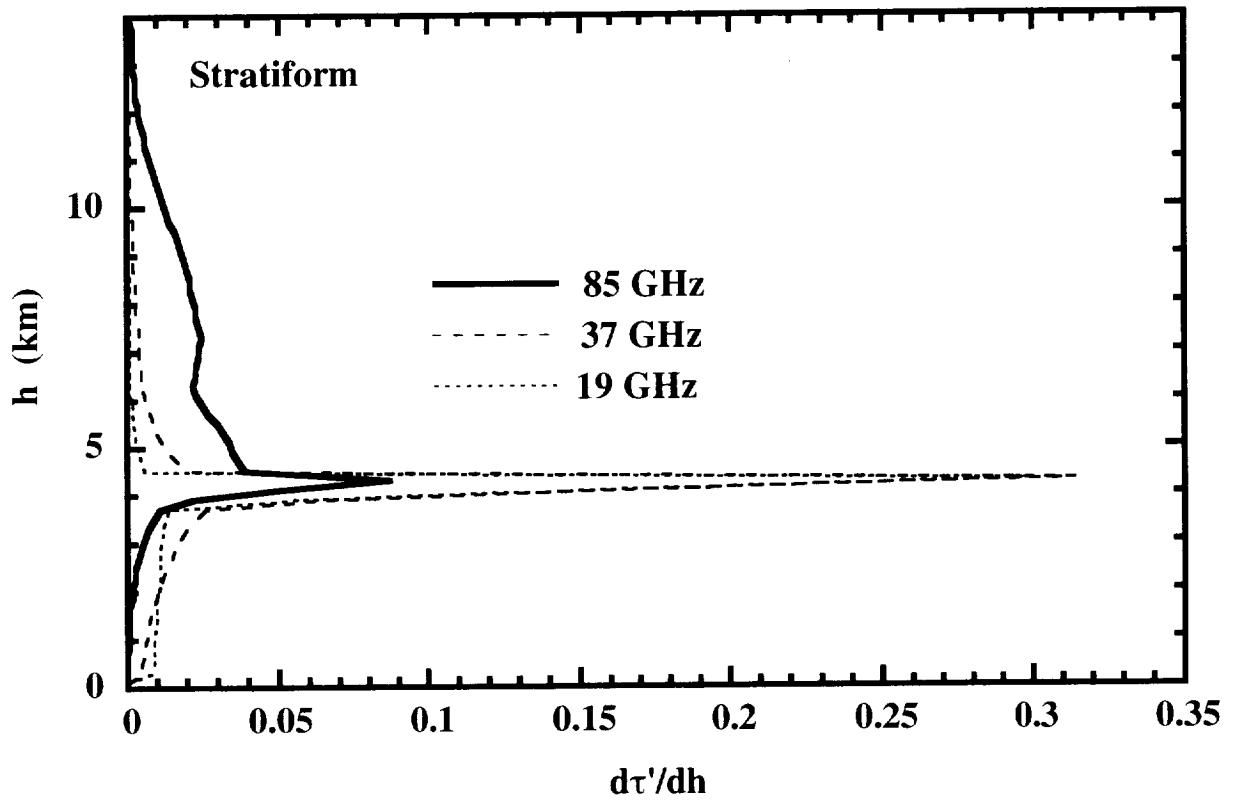
Figure 15: The weighting functions for the stratiform region for the 85 GHz (dark solid line), 37 GHz (dashed line), and 19 GHz (dotted line) channels. These weighting functions are derived using the $\overline{Z}$ profile in Table 2b Row C. Also, the parameter N^* is 10^6 m^{-4}.

observed and simulated T37 and T19 cannot be explained by the simple radiative transfer models implemented here. We deduce from these observations that the radiative properties of the bright band in the model for 37 and 19 GHz are critical in simulating T37 and T19. Also, the problems introduced by the differences in the viewing geometry of PR and TMI are more acute in the regions where the rain rates are weak (see Fig. 5a). Furthermore, we may point out that the problems present in the simulation of T19 and T37 are not eliminated by taking the difference T19-T37. However, T19-T37 obtain from observation show a fair correlation with the rain rate.

In this study, we find that the melting of snow flakes in these simulations results in a decreased brightness temperature over the land of about 10, 5 and 1 K for T19, T37 and T85, respectively. From the calculations of Bauer et al. (2000), applicable to oceanic regions, they found that the brightness temperature at 19 GHz increases by about 30 K, while at 85 GHz this increase is less than 8 K. Taking into consideration the difference in surface emissivity over land and ocean, theoretical results from both studies display a fair consistency.

4.C. Review of Simulations

From the radiative transfer simulations presented above using convective models, we conclude that it is possible to crudely explain the interrelationship between Tbs, observed in the 85, 37 and 19 GHz, by the radiometer, and reflectivity measured by the radar. However, as pointed out above, on a 20 km scale the horizontal inhomogeneities in the rain areas and the difference in the viewing geometry of the radar and radiometer can introduce discrepancies between observed and simulated Tbs.

44

The treatment of the melting layer in the stratiform region is very critical for the 19 and 37 GHz channels, and this could lead to some discrepancy. These discrepancies cannot be resolved purely with the help of the available radar and radiometer data.

Since the radiometer measured brightness temperatures respond to the various hydrometeors contained in a total column in the atmosphere, the corresponding near-surface rain rate estimated from the PR will show considerable amount of scatter, as shown in Fig. 3a. On the other hand, when sufficient averaging is applied to the radar and radiometer data, it is possible to relate rain rate to the brightness temperature, as shown in Fig. 3b.

As stated earlier, the relatively pure convective and stratiform rain *pixels* of 20 km scale constitute on average only about 15 % of the total number of rain *pixels* in a given MCS. The other 85 % of the data are less pure. Based on this study, we infer that the Tbs corresponding to this intermediate category will have a relationship with rain rate that falls in between the relationships for relatively pure convective and stratiform *pixels*.

In this study, we have attempted to relate the PR reflectivity profiles with the TMI measured brightness temperatures including the mixed layer in the convective model. In the stratiform model, allowance is made for a melting layer, or bright band. In some earlier studies - i.e., Viltard et al. (2000), Bennartz and Petty (2001), and Kummerow (2001) - these details were not incorporated into their radiative transfer models.

As we had stated earlier in Section 3 (see Eq. 5), the rain rate deduced from PR reflectivity depends on the PSD. In this study, to simulate the observed brightness temperatures, we found that suitable values of N_0 in the convective model and N^* in the stratiform model are 2×10^6 m^{-4} and 10^6 m^{-4}, respectively. The rain rates derived with these values of N_0 and N^* differ systematically by about 20 % from the PR rain rates. The reason for this difference is that a Gamma PSD is used to estimate PR rain rates (see Iguchi et al., 2000), while we used a Marshall-Palmer DSD in our study.

Detailed sensitivity results to the following variables have not been explicitly demonstrated: 1) density of graupel and ice aggregates, 2) surface temperature, and 3) relative shape of the ice particles. For an ice particle with a given mass, when the density of the ice particle is increased, scattering is enhanced. For a given lapse rate in the atmosphere, when the surface temperature is increased, the upwelling brightness temperatures are also increased. Based on earlier studies (e.g., Wu and Weinman, 1984), the difference between the brightness temperatures in the horizontal and vertical polarization could be effected by the shape of the ice particles more sensitively than the magnitude of the individual brightness temperatures. Even though we have not fully considered these sensitivities, we contend that it is feasible to simulate crudely the interrelationship between the brightness temperatures observed by TMI and the vertical profile of reflectivity derived by PR with the convective and stratiform models of microwave radiative transfer developed here.

5. Conclusions

Hydrometeor distributions associated with rain are highly variable in space and time. Understanding the impact of hydrometeor profiles on radiative transfer with the help of observations and models is needed in developing rainfall retrieval methods from microwave radiometer data. For this purpose, in this study we have examined the information given by the PR and TMI onboard the TRMM satellite for relatively pure convective and stratiform rain regions. For the purpose of comparison, it helps to average the radar and radiometer data to a scale of about 20 km, because the PR and TMI have different viewing geometry. The average properties of the PR and TMI data presented in Tables 2a and 2b, based on 20 MCS cases over tropical land, are very helpful to understand the observations from these two instruments. These tables, and Figs. 4a and 4b, show that on average there is a relationship between the PR reflectivity profiles and TMI measured brightness temperatures in 85, 37, and 19 GHz. Also, TMI and PR observations in the tropics show that there are distinctly different relationships between T85 and PR rain rate for the convective and stratiform rain regions. As shown in Fig. 3b, for a given change in rain rate, T85 varies much less in convective regions than in stratiform regions. On the other hand, from Tables 2a and 2b, one finds that the radiometer data in 19, 37, and 85 GHz channels are on the average redundant and have a poor ability to estimate convective and stratiform rain rates in an objective fashion. Thus, any method to retrieve rain rate from a microwave radiometer must have a technique to separate convective and stratiform rain areas. One such method to discriminate these areas depends on local minima in the spatial distribution of 85 GHz data (see PIWD, 2000).

In order to explain the relationship between TMI measured brightness temperatures and PR reflectivity profiles (see Figs. 4a and 4b), we have performed radiative transfer calculations. In these calculations, it is found that it is necessary to include a mixed layer of water drops and ice particles in the convective rain regions above the freezing level, and a melting layer (bright band) in the stratiform regions below the freezing level. Also, the hydrometeor particle size distribution is found to play an important role in both the convective and stratiform simulations. In Section 4, we show from theoretical simulations that because of errors introduced by differences in the viewing geometry, it is possible to explain only crudely the observed brightness temperatures in the 85 GHz channel for both convective and stratiform regions. Furthermore, the 19 and 37 GHz channels can also be crudely simulated for the convective regions, but they cannot be simulated equally well for the stratiform regions. Problems arising from the melting layer and contamination introduced by the relatively warm surface and the lower layers in the atmosphere force the simulated values to differ from the observed values in the stratiform regions.

From Fig. 1d, we infer that the surface and lower atmospheric contamination in the long wavelengths can be minimized by taking the difference between brightness temperatures in the 19 and 37 GHz channels, i.e. T19-T37. This difference signal, although weaker in magnitude, has a similar relationship with rain rate as that of T85. This suggests that T19-T37 may be used as additional information to enhance rain information from TMI.

Liu and Curry (1998, 1999, and 2000) show from the aircraft and satellite passive microwave radiometer data that channels near 150 GHz, which have much stronger

extinction than the 85 GHz, can give useful information about ice water content in the upper layers of the troposphere. Because of its higher frequency, for the same size of antenna, a channel near 150 GHz can yield a spatial resolution that is about two times better than the 85 GHz. We find that this high extinction and spatial resolution will be extremely valuable in isolating brightness temperature minima corresponding to convective cells in vigorously developing and decaying thunderstorms (PIWD, 2000). Also, 150 GHz radiation is more opaque to water vapor than that at 85 GHz. This makes a 150 GHz channel useful in the middle and high latitudes, where surface contamination becomes a problem at 85 GHz. From these considerations, we contend that microwave radiometers with a conical-scanning geometry that yields spatially continuous observations in a 150 GHz channel will be valuable for the remote sensing of rain.

Understanding the relationship between the measurements made by microwave radiometers and convective and stratiform rain is necessary for the future Global Precipitation Measurement (GPM) mission (E. A. Smith, personal communication). In GPM a constellation of satellites with microwave radiometers are expected to be flown without an accompanying radar. This will also be the case with microwave radiometers onboard the Earth Observing System's Aqua satellite and the Japanese satellite Adeos. Thus, the present study has useful applications for future satellite missions.

Acknowledgments

Appendix: Computational Model of Radiative Transfer

Assuming local thermodynamic equilibrium and plane-parallel stratification, the radiative transfer equation, including absorption and scattering processes in the atmosphere, can be written as follows at a given frequency of radiation in the microwave region (Chandrasekhar, 1960; Weinman and Guetter, 1977):

$$-\mu \frac{dT_b(\tau,\mu)}{d\tau} = -T_b(\tau,\mu) + \frac{\omega(\tau)}{2}\int_{-1}^{+1} P(\mu,\mu')T_b(\tau,\mu')d\mu' + \{1-\omega(\tau)\}T(\tau). \qquad (A.1)$$

The parameters in this equation are:

- $T_b(\tau,\mu)$ - the brightness temperature of radiation along a direction given by the direction cosine μ at an optical depth τ in the atmosphere.

- ω - the single scattering albedo, including cloud liquid, hydrometeors, and atmospheric gases, can be written as $\omega(\tau) = k_s/(k_s + k_a + k_g) = k_s/k_e$, where k_s, k_a, and k_e are the volume scattering, absorption, and extinction coefficients of the particles. Furthermore, k_g represents the total volume absorption coefficient due to gases in the atmosphere.

- $P(\mu,\mu')$ - the azimuthally averaged scattering phase function. The symbol μ' represents the direction cosine of incident radiation.

- $T(\tau)$ - the local temperature of the atmosphere.

The two boundary conditions to solve Eq. A.1 are the brightness temperature downwelling on the top of the atmosphere, and upwelling at the bottom of the atmosphere. These are given below:

$$T_b\left(\tau = 0, \mu^-\right) = 3\,\text{K} \tag{A.2a}$$

$$T_b\left(\tau = \tau_s, \mu^+\right) = T_s \varepsilon_s(\mu) + \left\{1 - \varepsilon_s(\mu)\right\} T_b\left(\tau = \tau_s, \mu^-\right), \tag{A.2b}$$

where $T_b\left(\tau = \tau_s, \mu^-\right)$ is the downwelling brightness temperature incident on the surface. The parameters T_s and $\varepsilon_s(\mu)$ are the surface temperature and emissivity, respectively.

In our model, this atmosphere is numerically represented with 90 layers between the surface and an altitude of 18 km. We solve Eq. A.1 numerically by the method of successive orders of scattering. This method involves computation of the source function and intensity using the recursion relationship between them (see for e.g. Liou, 1980; Prabhakara et al., 1988) for each successive order of scattering. In this study, the method is iterated until the brightness temperature emerging at the top of the atmosphere converges to within 0.1 K.

We have used the Mie computational procedure of Wiscombe (1980) to calculate the volume absorption and scattering coefficients, k_a and k_s, as well as the phase function, **P**. We may note these properties k_a, k_s and **P** depend on the real and imaginary parts of the refractive index as a function of the local temperature (Ray, 1972).

When a given volume of the atmosphere contains both water drops and ice particles, k_s, k_e, and $P(\mu,\mu')$ are defined by

$$k_s = f_{wat}k_{swat} + f_{ice}k_{sice}$$
$$k_e = f_{wat}k_{ewat} + f_{ice}k_{eice}$$
$$P(\mu,\mu') = f_{wat}P_{wat}(\mu,\mu') + f_{ice}P_{ice}(\mu,\mu').$$

(A.3)

The volume fractions of water, f_{wat}, and ice, f_{ice}, are defined in Eq. 6 of the text. Also, in the above equation k_{swat}, k_{ewat}, and $P_{wat}(\mu,\mu')$ are respectively the scattering and extinction coefficients and the phase function for water. Similarly, k_{sice}, k_{eice}, and $P_{ice}(\mu,\mu')$ are the scattering and extinction coefficients and the phase function for ice, respectively.

In Eq. A.1, the sum of the two terms farthest to the right are referred to as the source function. Thus, the source function, $S(\tau,\mu)$, is expressed as:

$$S(\tau,\mu) = \frac{\omega(\tau)}{2}\int_{-1}^{+1}P(\mu,\mu')T_b(\tau,\mu')d\mu' + \{1 - \omega(\tau)\}T(\tau).$$

(A.4)

When the scattering in the atmosphere is absent, the source function reduces to $T(\tau)$.

References

Adler, R. F. and A. J. Negri, 1988: A satellite infrared technique to estimate tropical convection and stratiform rainfall. *J. Appl. Met.*, **27**, 30-51.

Balakrishnan, N. and D. S. Zrnic, 1990: Estimation of rain and hail rates in mixed-phase precipitation. *J. Atmos. Sci.*, **47**, 565-583.

Bauer, P., A. Khain, A. Pokrovsky, R. Meneghini, C. Kummerow, F. Marzano, and J. P. V. Poiares Baptista, 2000: Combined cloud-microwave radiative transfer modeling of stratiform rainfall. *J. Atmos. Sci.*, **57**, 1082-1104.

Bennartz, R. and G. W. Petty, 2001: The sensitivity of microwave remote sensing observations of precipitation to ice particle size distributions. *J. Appl. Met.*, **40**, 345-364.

Bringi, V. N., K. Knupp, A. Detwiler, L. Lui, I. J. Caylor, and R. A. Black, 1997: Evolution of a Florida thunderstorm during the Convective and Precipitation/ Electrification Experiment: The case of 9 August 1991. *Mon. Wea. Rev.*, **125**, 2131-2160.

Chandrasekhar, S., 1960: *Radiative Transfer*, Dover, Inc., New York, 393 pp.

Hong, Y., J. L. Haferman, W. S. Olson, and C. D. Kummerow, 2000: Microwave brightness temperatures from tilted convective systems. *J. Appl. Meteor.*, **39**, 983-998.

Houze Jr., R. A., P. V. Hobbs, P. H. Herzegh, and D. B. Parsons, 1979: Size distributions of precipitation particles in frontal clouds. *J. Atmos. Sci.*, **36**, 156-162.

Houze Jr., R. A., 1993: *Cloud Dynamics*. Academic Press, Inc., San Diego, 571 pp.

Houze Jr., R. A., 1997: Stratiform precipitation in regions of convection: A meteorological paradox? *Bull. Amer. Met. Soc.*, **78**, 2179-2196.

Iguchi, T., T. Kozu, R. Meneghini, J. Awaka, and K. Okamoto, 2000: Rain-profiling algorithm for the TRMM Precipitation Radar. *J. Appl. Met.*, **39**, 2038-2052.

Kummerow, C., Y. Hong, W. S. Olson, S. Yang, R. F. Adler, J. McCollum, R. Ferraro, G. Petty, D.-B. Shin, and T. T. Wilheit, 2001: The evolution of the Goddard Profiling Algorithm (GPROF) for rainfall estimation from passive microwave sensors. *J. Appl. Met.*, **40**, 1801-1820.

Liao, L. and R. Meneghini, 2000: Investigation of the dielectric contant of inhomogeneous air-ice and snow-water spheres. IGARSS.

Liou, K., 1980: *An Introduction to Atmospheric Radiation*. Academic Press, Inc., Orlando, 392 pp.

Liu, G. and J. A. Curry, 1998: Remote sensing of ice water characteristics in tropical clouds using aircraft microwave measurements. *J. Appl. Met.*, **37**, 337-355.

Liu, G. and J. A. Curry, 1999: Tropical ice water amount and its relations to other atmospheric hydrological parameters as inferred from satellite data. *J. Appl. Met.*, **38**, 1182-1194.

Liu, G. and J. A. Curry, 2000: Determination of ice water path and mass median particle size using multi-channel microwave measurements. *J. Appl. Met.*, **39**, 1318-1329.

Meneghini, R. and L. Liao, 1996: Comparisons of cross sections for melting hydrometeors as derived from dielectric mixing formulas and a numerical method. *J. Appl. Met.*, **35**, 1658-1670.

Meneghini, R. and L. Liao, 2000: Effective dielectric constants of mixed-phase hydrometeors. *J. Atm. Oceanic Tech.*, **17**, 628-640.

Magono, C., and T. Nakamura, 1965: Aerodynamic studies of falling snowflakes. *J. Met. Soc. Japan*, **43**, 139-147.

Prabhakara, C., R. S. Frasier, G. Dalu, M.-L. C. Wu, R. J. Curran, T. Styles, 1988: Thin cirrus clouds: Seasonal distribution over oceans deduced from Nimbus-4 IRIS. *J. Appl. Met.*, **27**, 379-399.

Prabhakara C., R. Iacovazzi, Jr., J. A. Weinman, and G. Dalu, 2000: A TRMM microwave radiometer rain rate estimation method with convective and stratiform discrimination. *J. Met. Soc. Japan*, **78**, 241-258.

Ray, P. S., 1972: Broadband complex refractive indicies of ice and water. *Appl. Optics*, **11**, 1836-1843.

Sax, R. I. and V. W. Keller, 1980: Water-ice and water-updraft relationships near −10°C with populations of Florida cumuli. *J. Appl. Met.*, **19**, 505-514.

Schols, J. L., J. A. Weinman, G.D. Alexander, R. E. Stewart, L.J. Angus, and A.C.L. Lee, 1999: Microwave properties of frozen precipitation around a North Atlantic cyclone. *J. Appl. Met.*, **38**, 29-43.

Sekhon, R. S. and R. C. Srivastava, 1970: Snow size spectra and radar reflectivity. *J. Atmos. Sci.*, **27**, 299-307.

Short, D. A., P. A. Kucera, B. S. Ferrier, J. C. Gerlach, S. A. Rutledge, and O. W. Thiele, 1997: Shipboard radar rainfall patterns within the TOGA COARE IFA. *Bull. Amer. Met. Soc.*, **78**, 2817–2836.

Smith, P. L., D. J. Musil, A. G. Detwiler, and R. Ramachandran, 1999: Observations of mixed-phase precipitation within a CaPE thunderstorm. *J. Appl. Met.*, **38**, 145-155.

Ulaby, F. T., R. K. Moore, and A. K. Fung, 1981: *Microwave Remote Sensing: Active and Passive - Volume I: Microwave Remote Sensing Fundamentals and Radiometry.* Artech House, Norwood, MA, 456 pp.

Viltard, N., C. Kummerow, W. S. Olson, and Y. Hong, 2000: Combined use of the radar and radiometer of TRMM to estimate the influence of drop size distribution on rain retrievals. *J. Appl. Met.*, **39**, 2103-2114.

Weinman, J. A. and P. J. Guetter, 1977: Determination of rainfall distributions of microwave radiation measured by the Nimbus 6 ESMR. *J. Appl. Met.*, **16**, 437-442.

Wiscombe, W., 1980: Improved Mie scattering algorithms. *Appl. Opt.*, **19**, 1505-1509.

Wu, R. and J. A. Weinman, 1984: Microwave radiances from precipitating clouds containing aspherical ice, combined phase, and liquid hydrometeors. *J. Geophy. Res.*, **89**, 7170-7178.

REPORT DOCUMENTATION PAGE

Form Approved
OMB No. 0704-0188

1. AGENCY USE ONLY *(Leave blank)*	2. REPORT DATE February 2002	3. REPORT TYPE AND DATES COVERED Technical Memorandum

4. TITLE AND SUBTITLE
Simulation of TRMM Microwave Imager Brightness Temperature Using Precipitation Radar Reflectivity for Convective and Straitform Rain Areas Over Land

5. FUNDING NUMBERS
Code 913.0

6. AUTHOR(S)
C. Prabhakara, R. Iacovazzi, Jr., and J.-M. Yoo

7. PERFORMING ORGANIZATION NAME(S) AND ADDRESS (ES)
Goddard Space Flight Center
Greenbelt, Maryland 20771

8. PEFORMING ORGANIZATION REPORT NUMBER
2002-01042-0

9. SPONSORING / MONITORING AGENCY NAME(S) AND ADDRESS (ES)
National Aeronautics and Space Administration
Washington, DC 20546-0001

10. SPONSORING / MONITORING AGENCY REPORT NUMBER
TM-2002-210000

11. SUPPLEMENTARY NOTES

R. Iacovazzi, Jr.: Science Systems and Applications, Inc., Lanham, MD
J.-M. Yoo: EWHA Womans University, Seoul, South Korea

12a. DISTRIBUTION / AVAILABILITY STATEMENT
Unclassified–Unlimited
Subject Category: 43 and 47
Report available from the NASA Center for AeroSpace Information,
7121 Standard Drive, Hanover, MD 21076-1320. (301) 621-0390.

12b. DISTRIBUTION CODE

13. ABSTRACT *(Maximum 200 words)*

Rain is highly variable in space and time. In order to measure rainfall over global land with satellites, we need observations with very high spatial resolution and frequency in time. On board the Tropical Rainfall Measuring Mission (TRMM) satellite, the Precipitation Radar (PR) and Microwave Imager (TMI) are flown together for the purpose of estimating rain rate. The basic method to estimate rain from PR has been developed over the past several decades. On the other hand, the TMI method of rain estimation is still in the state development, particularly over land. The objective of this technical memorandum is to develop a theoretical framework that helps relate the observations made by these two instruments. The principle result of this study is that in order to match the PR observations with the TMI observations in convective rain areas, a mixed layer of graupel and super-cooled water drops above the freezing level is needed. On the other hand, to match these observations in the straitform region, a layer of snowflakes with appropriate densities above the freezing level, and a melting layer below the freezing level, are needed. This understanding can lead to a robust rainfall estimation technique from the microwave radiometer observations.

14. SUBJECT TERMS
radiative transfer simulations, passive microwave radiometer, TRMM, convective rain, straitform rain, melting layer, mixed phase layer

15. NUMBER OF PAGES
63

16. PRICE CODE

17. SECURITY CLASSIFICATION OF REPORT Unclassified	18. SECURITY CLASSIFICATION OF THIS PAGE Unclassified	19. SECURITY CLASSIFICATION OF ABSTRACT Unclassified	20. LIMITATION OF ABSTRACT UL